Atmos. Chem. Phys. Discuss., 12, 23829–23911, 2012
www.atmos-chem-phys-discuss.net/12/23829/2012/
doi:10.5194/acpd-12-23829-2012

Atmospheric Chemistry and Physics Discussions

An empirical model of global climate – Part 1: Reduced impact of volcanoes upon consideration of ocean circulation

T. Canty[1], **N. R. Mascioli**[1], **M. Smarte**[2], **and R. J. Salawitch**[1,2,3]

[1]Department of Atmospheric and Oceanic Science, University of Maryland, College Park, MD, USA
[2]Department of Chemistry and Biochemistry, University of Maryland, College Park, MD, USA
[3]Earth System Science Interdisciplinary Center, University of Maryland, College Park, MD, USA

Received: 21 July 2012 – Accepted: 24 August 2012 – Published: 13 September 2012

Correspondence to: T. Canty (tcanty@atmos.umd.edu)

Published by Copernicus Publications on behalf of the European Geosciences Union.

Abstract

Observed reductions in Earth's surface temperature following explosive volcanic eruptions have been used as a proxy for geo-engineering of climate by the artificial enhancement of stratospheric sulfate. Earth cools following major eruptions due to an increase in the reflection of sunlight caused by a dramatic enhancement of the stratospheric sulfate aerosol burden. Significant global cooling has been observed following the four major eruptions since 1900: Santa María, Mount Agung, El Chichón, and Mount Pinatubo, leading IPCC (2007) to state "major volcanic eruptions can thus cause a drop in global mean surface temperature of about half a degree Celsius that can last for months and even years". We use a multiple linear regression model applied to the global surface temperature anomaly to suggest that exchange of heat between the atmosphere and ocean, driven by variations in the strength of the Atlantic Meridional Overturning Circulation (AMOC), has been a factor in the decline of global temperature following these eruptions. The veracity of this suggestion depends on whether the Atlantic Multidecadal Oscillation (AMO) truly represents a proxy for the strength of the AMOC and the precise quantification of global cooling due to volcanoes depends on how the AMO is detrended. If the AMO is detrended using anthropogenic radiative forcing of climate, we find that surface cooling attributed to Mount Pinatubo, using the Hadley Centre/University of East Anglia surface temperature record, maximizes at 0.15 °C globally and 0.35 °C over land. These values are about a factor of 2 less than found when the AMO is neglected in the model and quite a bit lower than the canonical 0.5 °C cooling usually attributed to Pinatubo. The AMO had begun to decrease prior to the four major eruptions, suggesting that exchange of heat between the atmosphere and ocean due to variations in the strength of the AMOC drives the climate system, rather than responds to volcanic perturbations. The satellite record of atmospheric temperature from 1978 to present and other century-long surface temperature records are also consistent with our suggestion that volcanic cooling may have been over estimated by about a factor of 2 due to prior neglect of ocean circulation. Finally,

ACPD

12, 23829–23911, 2012

a regression using AMO simulates pre-WWI cooling and WWII warming of global temperature particularly well, supporting the possibility that variations in the strength of the AMOC have truly exerted influence on global climate.

1 Introduction

It is well established that both natural and anthropogenic factors influence climate. Natural factors include variations in the intensity of sunlight driven by the ∼11 yr cycle of solar activity, variations in exchange of heat between the atmosphere and Pacific Ocean following the shift in ocean circulation recorded by the El Niño-Southern Oscillation (ENSO), and periodic volcanic eruptions with enough energy to dramatically enhance the stratospheric aerosol burden (e.g. Mass and Portman, 1989; Sects. 2.7 and 3.6.2 of IPCC, 2007; Lean and Rind, 2008). Anthropogenic factors include increases in the radiative forcing at the tropopause (RF) due to rising levels of greenhouse gases (GHGs) that cause the lower atmosphere to warm as well as the industrial release of precursors of tropospheric aerosols that can cause the lower atmosphere to either cool or warm, depending on a myriad of factors (Sect. 2.4 of IPCC, 2007). Throughout, we use RF to refer to the stratospheric-adjusted RF described in Sect. 2.2 of IPCC, 2007.

Atmosphere ocean general circulation models (GCMs) are commonly used to quantify the relative importance of natural (i.e. volcanoes and ocean circulation) and anthropogenic (i.e. GHGs and tropospheric aerosols) factors on global climate. Soden et al. (2002) used a GCM to show that the 0.5 °C cooling of the global lower troposphere, measured by the Microwave Sounding Unit (MSU) after the eruption of Mount Pinatubo (hereafter, Pinatubo), was well simulated provided: (a) there is a significant positive feedback due to changes in atmospheric H_2O, in response to the perturbation of the shortwave (SW) solar and longwave (LW) thermal radiation fields induced by Pinatubo; (b) the MSU data record is adjusted for a ∼0.2 °C warming due to ENSO. The need for a significant climate feedback to quantitatively account for the temperature perturbation following the Pinatubo eruption was also discussed by Hansen

ACPD
12, 23829–23911, 2012

et al. (1993), Lacis and Mischenko (1995), Forster and Collins (2004), and Wigley et al. (2005a).

Multiple linear regression (MLR) of the global surface temperature anomaly (ΔT) has also been used to quantify the relative importance of natural and anthropogenic factors on climate (Lean and Rind, 2008, 2009; Kopp and Lean, 2011). Typically, coefficients are found that relate a time series of ΔT to the temporal variation of proxies that represent RF due to total solar irradiance (TSI), volcanoes, ENSO, and anthropogenic radiative forcing of climate (AF) due to GHGs and aerosols. Time series of stratospheric optical depth (SOD), available for the past century from one of two independent analyses (Sato et al., 1993; Ammann et al., 2003; see Fig. 2.18 of IPCC, 2007) are used to represent the volcanic term. Lean and Rind (2008) used an MLR analysis to estimate that Pinatubo caused a ~0.3 °C cooling of global surface temperature, considerably smaller than the canonical 0.5 °C cooling of global mean surface temperature commonly attributed to Pinatubo (e.g. Crutzen, 2006; IPCC, 2007, p. 97).

Here we conduct a MLR analysis of the global temperature record from 1900 to present. Our model uses as input globally averaged mixing ratios for greenhouse gases from the Representative Concentration Pathways (RCP) database provided for the upcoming IPCC report (Meinshausen et al., 2011; van Vuuren et al., 2011). Mixing ratios of GHGs are essentially identical in the four RCP scenarios, for our period of interest, 1900 to present. Abundances from the RCP 8.5 scenario (Riahi et al., 2007, 2011) are used. Results would be unchanged had a different scenario been chosen; the abundance of GHGs differs very slightly between the scenarios starting in 2005 (CH_4 and N_2O) and 2008 (CO_2). In our companion paper, Mascioli et al. (2012), we examine the sensitivity of future climate to the four RCP scenarios, which diverge strongly for GHGs midway through this century.

The start date of year 1900 for our analysis allows examination of perturbations to global climate following the major eruptions of Santa María (October 1902), Mount Agung (March 1963), El Chichón (April 1982), and Mount Pinatubo (June 1991) and all minor eruptions strong enough to affect stratospheric optical depth, but precludes

ACPD
12, 23829–23911, 2012

examination of perturbations due to eruptions of Tambora in 1815 and Krakatoa in 1883. Data needed for our analysis becomes more scarce and uncertain prior to 1900. Also, some of the key figures in IPCC (2007) important for to our work, such as Figs. TS.23 and 9.14, begin around 1900. Finally, our time period covers the same set of major volcanic eruptions examined by Wigley et al. (2005a).

In addition to the commonly used regressor variables SOD, TSI, Anthropogenic RF, and ENSO, we introduce to the regression proxies representing variations in the strength of the Atlantic Meridional Overturning Circulation (AMOC), the Pacific Decadal Oscillation (PDO), and the Indian Ocean Dipole (IOD). The de-trended Atlantic Multi-decadal Oscillation (AMO) index is used as a proxy for the strength of the AMOC (Andronova and Schlesinger, 2000; Knight et al., 2005; Stouffer et al., 2006; Medhaug and Furevik, 2011). Throughout, we provide extensive discussion of AMOC and AMO, and little discussion of the PDO and IOD, because we compute small contributions of the PDO and IOD to variations of global temperature. Indeed, this is the basis upon which Schlesinger and Ramankutty (1994) first identified the global, climatic significance of multi-decadal variations of sea surface temperature (SST) in the North Atlantic basin. Below, we show that the expression of AMOC in the temperature record is found for a myriad of data sets, including surface observations (global and land) from four data centers as well as the modern satellite data record.

We find that global cooling attributed to volcanoes ($\Delta T_{\mathrm{VOLCANO}}$) declines sharply, by almost a factor of 2, when the AMO is introduced into the regression. Much of this paper focuses on the robustness of this result. We show that the precise value of $\Delta T_{\mathrm{VOLCANO}}$ depends on how SST in the North Atlantic, the basis for the AMO, is de-trended. Details of the various empirical parameters used in this analysis are provided in Sect. 2. A description of the model is given in Sect. 3. Results of the regression analysis are provided in Sect. 4. Discussion of these results, including a focus on the AMO and AMOC as well as implications for geo-engineering of climate, is provided in Sect. 5. A brief conclusion follows. Many abbreviations and symbols are used; although each is defined, a Glossary of terms is provided in Appendix A. Appendix B contains

ACPD
12, 23829–23911, 2012

web addresses (URLs) for the many sources of data used in the analysis. Appendix C describes calculation of the statistical uncertainty of the regression coefficients and Appendix D details how we have arrived at an estimate for the empirical range of net anthropogenic aerosol radiative forcing (NAA RF) from IPCC (2007).

2 External sources of data

This study uses many sources of data. We describe here data used in the manner it was provided: i.e., data obtained from external websites and used without further processing. Data records that require internal processing, such as the index for the AMO and the terms used to define anthropogenic RF of climate, are described in Sect. 3 (Model description). We envision this section as a "boiler plate" description of data sets used in their original form and Sect. 3 as a description of how our model was constructed.

2.1 Global temperature

Our regression model, described in Sect. 3, uses as input monthly, mean near surface air (hereafter, surface) surface temperature anomalies (either global or land) ($\Delta T_{\mathrm{OBS}\ i}$) and the 1-sigma uncertainties of each monthly measurement ($\sigma_{\mathrm{OBS}\ i}$). Some of the papers and/or data files provide 2-sigma uncertainties: if so, we have multiplied these values by 0.5 to obtain an estimate of the 1-sigma measurement uncertainty. Throughout, the use of bold-faced, as for CRU4 below, denotes that a web-link for this data source is provided in Appendix B.

2.1.1 Surface

CRU4: the Climate Research Unit (CRU) of the University of East Anglia together with the Hadley Centre of the UK Met Office provide a global, monthly mean surface temperature (Morice et al., 2012) and land temperature (Jones et al., 2012) record. We

ACPD
12, 23829–23911, 2012

are using the most recent version of each data set available at the time of submission: HadCRUT4 for global and CRUTEM4 for land. These data sets are provided on different websites. Below, we refer to both HadCRUT4 and CRUTEM4 as CRU4, with clear notation for global or land. The land record is based on data from 5583 stations. The global record combines this information with a SST record based on ship and buoy observations from the International Comprehensive Ocean-Atmosphere Data Set (ICOADS).

The HadCRUT4 data incorporates an SST data set that is termed HadSST3 (Kennedy et al., 2011a,b). HadSST3 accounts for ocean sampling bias described by Thompson et al. (2008). The HadSST3 data set is used for our various definitions of AMO (Sect. 3.2.2).

Both HadCRUT4 and CRUTEM4 time series represent anomalies relative to the mean value of ΔT_{OBS} from 1961 to 1990. The uncertainties for HadCRUT4 are provided in data files accessible from the website noted in Appendix B. Uncertainties for CRUTEM4 were obtained from Jones et al. (2012).

These CRU4 records are the only data set used for our "ladder plots" that compare modeled and measured surface ΔT. We have chosen CRU4 for these plots due to the prominence placed on this record by IPCC (2007). Other data sets for global and land ΔT are used for our quantification of the sensitivity of $\Delta T_{\mathrm{VOLCANO}}$ to AMO, and are represented in summary figures and tables.

GISS: the Goddard Institute for Space Studies (GISS) provides a climate record that is based on SST from a combination of the Hadley Centre analysis (HadISST1) for 1880 to 1982 and satellite observations for 1982 to present (Hansen et al., 2010) and land temperature from over 700 surface meteorological stations that are part of Global Historical Climatology Network-Monthly (GHCN-M). Data from GISS are available from prior to 1900 until the end of 2011. Uncertainty estimates for the global temperature are from Hansen et al. (2006) and for land are from Hansen et al. (2010). Values of ΔT from GISS are presented as the anomaly with respect to 1951 to 1980. The use of a different time period for the anomaly, compared to CRU4, affects only the constant

ACPD
12, 23829–23911, 2012

term (variable C_0 in Eq. (2) below) in the regression, and is therefore of no significance for the present analysis.

NCDC: the National Climate Data Center also provides global and land ΔT, from prior to 1900 until the end of 2011 (Smith et al., 2008). The land temperature anomalies are based on GHCN-M and SST is from ICOADS. The uncertainty estimates for global ΔT are from Smith et al. (2008) and for land are from Smith and Reynolds (2005). This temperature record is presented as an anomaly relative to mean temperature from 1901 to 2000. We only show $\Delta T_{\mathrm{VOLCANO}}$ versus SOD for NCDC Land; the $\Delta T_{\mathrm{VOLCANO}}$ versus SOD relation for NCDC Global is virtually indistinguishable from similar relations using the global record from CRU4 and GISS.

BEG: the Berkeley Earth Group provides an estimate of ΔT over land, from prior to 1800 to May 2010, based on measurements from 39390 unique meteorological stations (Rohde et al., 2011). The difference between the estimate for ΔT from BEG and the estimate from other data centers is that BEG uses data from many more sources. GHCN-M has strict criteria for record length, completeness, and establishment of a station baseline before data from a particular station becomes part of their record. The BEG has developed a methodology for the use of all data (Rohde et al., 2011). This record is available only for land at the present time. Uncertainties are provided in the BEG data file. The BEG temperature anomaly is relative to 1950 to 1980.

2.1.2 Atmosphere

MSU: the Microwave Sounding Unit (MSU) and the Advanced Microwave Sounding Unit (AMSU) provide measurements of atmospheric temperature, from December 1978 to present, from a series of National Oceanic and Atmospheric Administration (NOAA) satellites. We use the global LT5.4 (lower troposphere) product provided by the University of Alabama, Huntsville (Christy et al., 2000) and the land TLT product provided by Remote Sensing Systems (Appendix B). The MSU anomalies are relative to the mean temperature over the January 1979 to April 2002 period. Uncertainty estimates for MSU

ACPD
12, 23829–23911, 2012

are from Christy et al. (2003). The global MSU lower troposphere record shown below agrees well with data shown in Fig. 2 of Soden et al. (2002).

2.2 Regression variables

Here we describe the origin of variables used in the regression model that require no processing.

SOD, GISS: we use a monthly mean, globally averaged time series of stratospheric optical depth (SOD), available from 1850 to present from the Goddard Institute for Space Studies (GISS) (Sato et al., 1993) as a proxy for the volcanic perturbation to the stratospheric sulfate layer. This data set is based on ground, balloon-borne, and satellite observations. Satellite observations are available only from late 1978 to present. The scarcity of observing stations early in the record requires assumptions to be made regarding the geographic distribution of volcanic aerosols. We use the GISS record for SOD in the main body of our paper because it is the only SOD record regularly updated.

SOD, NOAA: a time series of monthly mean, globally averaged stratospheric optical depth (SOD) is also available from NOAA (Ammann et al., 2003). This time series is based on a 4-member ensemble simulation of volcanic eruptions, within a GCM that resolves the troposphere and stratosphere, to arrive at SOD. This record is available from 1890 to 2008. Figure 2.18 of IPCC (2007) compares the Sato et al. (1993) and Ammann et al. (2003) records for SOD. Generally, the peak SOD from Ammann exceeds the peak SOD from Sato after major volcanic eruptions. As shown in the Supplement, use of SOD from NOAA rather than SOD from GISS in our regression has no bearing on our finding regarding the sensitivity of $\Delta T_{\mathrm{VOLCANO}}$ to the AMO.

TSI: the total solar irradiance (TSI) time series used in our regression model is from the Naval Research Laboratory reconstruction of Lean (2000) and Wang et al. (2005). This data set is based on measurements from a variety of space-borne sensors starting in 1978, such as the Solar Stellar Irradiance Comparison Experiment on the Upper Atmosphere Research Satellite. For earlier periods of time, the reconstruction uses

ACPD
12, 23829–23911, 2012

information such as number, location, and darkening of sunspots as well as time series of Mg-II and Ca-II Fraunhofer lines recorded by ground based instruments. There has been recent debate over the absolute value of TSI (e.g. Kopp and Lean, 2011) as well as the variation of solar output in the ultraviolet (UV) at different phases of the 11 yr cycle (e.g. DeLand and Cebula, 2012; Lean and DeLand, 2012). Neither affects our study. The 11 yr periodicity of TSI is well established and the timing of the peaks and valleys are known. The regression model results are insensitive to the absolute value of TSI as well as variations of solar irradiance in the UV that have little consequence for TSI.

ENSO: we use the NOAA Multivariate El Niño-Southern Oscillation Index (ENSO) of Wolter and Timlin (2011). This index is derived from observations of cloud fraction, sea-level pressure, surface wind, sea surface temperature, and surface air temperature. Unlike other ENSO indices, such as those based on surface pressure, this ENSO index is dimensionless.

PDO: the Pacific Decadal Oscillation (PDO) represents the temporal evolution of specific patterns of sea level pressure and temperature of the Pacific Ocean, poleward of 20° N (Zhang et al., 1997), that have been shown to correlate with salmon, anchovy, and sardine populations in the Pacific (Chavez et al., 2003). We use a dimensionless index based on analysis of Empirical Orthogonal Functions of the SST anomaly conducted by the University of Washington (Zhang et al., 1997). The PDO is caused by the response of the ocean to spatially coherent atmospheric forcing (Saravanan and McWilliams, 1998; Wu and Liu, 2003). This may explain why the PDO has little influence on the global climate record: the PDO is a response to local wind patterns, rather than an indicator of major release (or uptake) of oceanic heat at a magnitude important for global climate.

IOD: the Indian Ocean Dipole (IOD) index represents the temperature gradient between the Western and Southeastern Equatorial Indian Ocean. We use an index, with units °C, provided by the Japan Agency for Marine-Earth Science and Technology (Saji et al., 1999). We have decided to show results using the IOD so that all three major

ACPD
12, 23829–23911, 2012

ocean basins are represented. There is little effect of the IOD on global climate, probably due to the size of the Indian Ocean as well as the fact that oceanic deep water does not originate from the Indian Ocean.

2.3 Atmospheric radiation

ERBE: we show satellite observations of perturbations to Earth's radiation budget following the eruption of Mt. Pinatubo, at shortwave (solar) wavelengths and longwave (thermal) wavelengths, as measured by Earth Radiation Budget Experiment (ERBE) instruments on three satellites: ERBS, NOAA-9, NOAA-10. The ERBE instrument measures incoming solar radiation, reflected shortwave radiation, and outgoing thermal radiation (Wielicki et al., 2002). We use Edition 3, Revision 1 ERBE data provided by the National Aeronautics and Space Administration, Langley Research Center, Atmospheric Science Data Center.

3 Model description

3.1 Model overview

Our MLR model builds on the work of Lean and Rind (2008) and Kopp and Lean (2011). However, our approach differs in four important manners.

First, we explicitly represent the increase in heat content of the upper 700 m of the global ocean (OHC) (Domingues et al., 2008; Carton and Santorelli, 2008; Church et al., 2011). This term was neglected in prior MLR studies.

Second, we quantify the sensitivity of the regression coefficients to uncertainty in NAA RF. Tropospheric aerosols that drive RF of climate can either cool (sulfate, dust, ammonium nitrate, organic carbon) or heat (black carbon) the lower atmosphere. Prior MLR studies, as well as many climate models, examine only a single scenario for NAA RF. Uncertainties in this term are quite large. We allow the regression to determine the best value of the climate sensitivity (via model parameter γ; described in Sect. 3.2) for

ACPD
12, 23829–23911, 2012

prescribed values of NAA RF and OHC. Quantification of the sensitivity of model parameters to uncertainty in NAA RF, even in a highly parameterized fashion, constitutes an important step forward.

Third, we conduct a weighted MLR that accounts for uncertainties of the climate record. Knowledge of ΔT has become better over time. As a result, the output of the regression model tends to follow the climate record more closely during the latter half of the century, which is the proper interpretation of the climate record upon consideration of time dependent uncertainties. We also compute the statistical uncertainty of the regression coefficients, although these terms are of limited utility.

Finally, in our regression model, we do not allow for multiple ENSOs offset in time (Kopp and Lean, 2011) or temporal shifts in the response of ΔT to ENSO, TSI, or Anthropogenic RF (Lean and Rind, 2008). The types of delays used in prior MLR analyses are not evident within GCMs (e.g. Fig. 3 of Solomon et al., 2010). We allow for a 6 month delay in the response of ΔT to volcanic perturbation of SOD. This lag is the same as used by Lean and Rind (2008) and agrees with the 6.8 ± 1.5 month lag estimated by Douglass and Knox (2005). Since the volcanic perturbation occurs in the stratosphere, and our model is based on stratospheric-adjusted RF (second panel, Fig. 2.2 of IPCC, 2007), this 6 month delay represents the time needed for the stratosphere to respond to a volcanically induced perturbation in sulfate aerosol loading.

3.2 Model details

Our regression model minimizes:

$$\text{Cost Function} = \sum_{i=1}^{N_{\text{MONTHS}}} \frac{1}{\sigma^2_{\text{OBS } i}} (\Delta T_{\text{OBS } i} - \Delta T_{\text{MDL } i})^2 \quad (1)$$

where $\Delta T_{\text{OBS } i}$ and $\Delta T_{\text{MDL } i}$ represent time series of observed and modeled global, monthly mean temperature anomalies, and $\sigma_{\text{OBS } i}$ is the 1-sigma uncertainty

ACPD
12, 23829–23911, 2012

associated with each temperature observation. We write $\Delta T_{\mathrm{MDL}\ i}$ as:

$$\Delta T_{\mathrm{MDL}\ i} = \lambda(1+\gamma)(\mathrm{GHG\ RF}_i) + \lambda(\mathrm{NAA\ RF}_i) + \mathrm{C}_0 + \mathrm{C}_1 \times \mathrm{SOD}_{i-6} + \mathrm{C}_2 \times \mathrm{TSI}_i + \mathrm{C}_3 \times \mathrm{ENSO}_i + \mathrm{C}_4 \times \mathrm{AMO}_i + \mathrm{C}_5 \times \mathrm{PDO}_i + \mathrm{C}_6 \times \mathrm{IOD}_i - \lambda \mathrm{Q}_{\mathrm{OCEAN}\ i} \quad (2)$$

where $\lambda = 0.3\,^{\circ}\mathrm{C/W\,m^{-2}}$ and i denotes month. We work exclusively in a global, monthly mean framework. Values of the regression coefficients ($\mathrm{C}_{j,\ j=0\ \mathrm{to}\ 6}$) and the sensitivity parameter in response to a GHG perturbation (γ) are found such that the cost function is minimized, for specified NAA RF_i and OHC (via model variable $Q_{\mathrm{OCEAN}\ i}$, described in Sect. 3.2.4) over the time period of consideration. Below, we show results for 1900 to the end of 2010 (ground-based observations of surface temperature) and 1978 to the end of 2011 (satellite observations of lower tropospheric temperature). The index $i-6$ for SOD represents the 6 month delay between volcanic forcing and surface temperature response (Douglass and Knox, 2005; Lean and Rind, 2008). Various volcanic eruptions could exhibit different lags due to the latitude of the eruption, which could drive hemispheric and/or latitudinal asymmetries in SOD, especially soon after the eruption (Wigley et al., 2005a). Our central result is essentially unchanged if we vary the lag time by ±1 month but does begin to change with larger shifts. For simplicity, we assume all eruptions exhibit the same 6 month lag.

This model framework relates anomalies in temperature to perturbations of stratospheric-adjusted RF (Sect 2.2 of IPCC, 2007). The term λ represents the response of surface temperature to a RF perturbation in the absence of any feedbacks, for Earth's present-day overall albedo. The numerical value corresponds to an Earth effective temperature of 245 K (Sect 1.4.4 of McGuffie and Henderson-Sellers, 2005) and is similar to values commonly used in other empirical analyses (e.g. Bony et al., 2006; Forster and Gregory, 2006; Soden and Held, 2006; Murphy et al., 2009).

IPCC (2007) as well as studies such as Bony et al. (2006), Forster and Gregory (2006), Soden and Held (2006), Knutti and Hegrel (2008), and Murphy et al. (2009)

ACPD
12, 23829–23911, 2012

use a definition for λ that is the inverse of our description: i.e., they base their models on RF = $\lambda\Delta T$ rather than $\Delta T = \lambda$ RF. In the RF = $\lambda\Delta T$ framework, feedbacks due to water vapor, clouds, or surface albedo can be expressed in an additive fashion (e.g. Soden and Held, 2006; Sect. 1.4.4 of McGuffie and Henderson-Sellers, 2005) and λ is called the climate feedback parameter (e.g. Knutti and Hegrel, 2008). In our framework, the term $\lambda(1+\gamma)$ is often called the climate sensitivity parameter (e.g. Knutti and Hegrel, 2008). We provide numerical values of γ on many of our figures because this is the parameter found using the MLR model. We also refer to γ as the "sensitivity parameter" since this term represents, physically, the sensitivity of climate to all feedbacks that occur in response to a GHG perturbation to RF. Should one decompose γ into component terms, the inverse of each term would be additive, i.e.:

$$\frac{1}{\gamma} = \frac{1}{\gamma_{\text{WATER VAPOR}}} + \frac{1}{\gamma_{\text{LAPSE RATE}}} + \frac{1}{\gamma_{\text{SURFACE ALBEDO}}} + \frac{1}{\gamma_{\text{CLOUDS}}} \quad (3)$$

(e.g., Eq. (12) of Hansen et al., 1984). However, we work exclusively with γ and do not consider component terms.

There are also important climate feedbacks that involve tropospheric aerosols (e.g., Fig. 2.10 of IPCC, 2007). Aerosol feedbacks are implicit in the scaling terms used to define NAA RF_i, which represents global, monthly mean total RF due to all anthropogenic aerosols including feedbacks. It is essential that the sensitivity of climate to a GHG perturbation (parameter γ) and tropospheric aerosols (parameters α_{COOL} and α_{HEAT} described in Sect. 3.2.2) be treated in an independent manner because: (a) the physical processes that link perturbation to response are extremely different for GHGs and aerosols; (b) the forcing of global climate due to tropospheric aerosols is projected to greatly diminish over the next century (Riahi et al., 2007, 2011).

The product of each regression coefficient ($C_{j,\ j=0\text{ to }6}$) and its associated regressor variable represents the contribution of this term to the global, monthly mean temperature anomaly. For instance, a time series of the effect of volcanoes on global temperature, $\Delta T_{\text{VOLCANO}\ i}$, is given by $C_1 \times \text{SOD}_{i-6}$ and the maximum temperature perturbation

ACPD
12, 23829–23911, 2012

due to Pinatubo, $\Delta T_{\text{PINATUBO}}$, is $C_1 \times 0.15$, because 0.15 is the maximum value of SOD observed after this eruption.

Values of the regression coefficients $C_{j,\ j=0 \text{ to } 6}$ are found using the Interactive Data Language (IDL®) program regress.pro. This program also provides an estimate of the uncertainty for each regression coefficient, which is used below for C_1 (Appendix C). As we show below, the value of C_1 depends not only on whether the AMO term is included in the model, but also on how the AMO has been detrended. The statistical uncertainty for C_1 provided by regress.pro for any particular calculation is small compared to the difference in C_1 found for various treatments of AMO. The built-in IDL uncertainty estimates, which represent a statistical uncertainty tied to $\sigma_{\text{OBS}\ i}$, do not consider uncertainties in the regressor variables (i.e. uncertainty in SOD, TSI, etc) or missing physics in the model. Hence, these statistical uncertainties are of limited utility. The AMO is the most important physical model parameter for our study, which is why we document the dependence of C_1 on various treatments of this term.

The origin of the SOD, TSI, ENSO, AMO, PDO, and IOD terms, which are all based on external sources of data, has been described in Sect. 2. The anthropogenic RF terms are described in Sects. 3.2.1 (GHGs) and 3.2.2 (Aerosols), the treatment of the AMO is detailed in Sect. 3.2.3, and the Ocean Heat Export is the focus of Sect. 3.2.4.

3.2.1 Anthropogenic radiative forcing: GHGs

Figure 1 shows time series of direct RF due to GHGs, a model input represented as GHG RF_i in Eq. (2). Monthly values of this forcing are specified from the RCP 8.5 scenario. We use global, annual mean mixing ratios of CO_2, CH_4, and N_2O provided on the **RCP** website (see Appendix B), which we interpolate to a monthly time grid. We then compute RF relative to year 1750 based on formula given in Table 6.2 of IPCC (2001).

The RF attributed to tropospheric O_3 is obtained directly from a radiative forcing file given on the **RCP Potsdam** website. The RF due to tropospheric O_3 given by RCP 8.5

ACPD
12, 23829–23911, 2012

compares reasonably well to the Shindell et al. (2006) value: the RCP values exceed the Shindell values from 1900 to about 1950, and the Shindell values exceed the RCP estimate for the last few decades. We have run some of our simulations using the Shindell et al. (2006) estimate for RF due to O_3, and the results are essentially identical to those shown here using RF due to O_3 from RCP 8.5.

The RF due to halocarbons shown in Fig. 1 is the sum of 30 compounds. For each compound, we have used global, yearly mixing ratios from either RCP 8.5 (Lamarque et al., 2010), Table 5A-3 of WMO (2011), or Velders et al. (2009) (updated by G. Velders, personal communication, 2011). Mixing ratios for HFC32, HFC125, HFC134a, HFC143a, HFC152a, HFC245fa, and HFC365mfc are from Velders. Mixing ratios for CFC11, CFC12, CFC113, CCl_4, HCFC141b, HCFC142b, Halon 1301, and Halon 2402 are from WMO (2011). All other halocarbons are from RCP 8.5. For each halocarbon, the RF term has been found using the formula given in Table 6.2 of IPCC (2001) combined with the radiative efficiency tabulation given in Table 2.14 of IPCC (2007). The use of mixing ratios from Velders et al. (2009) and from WMO (2011) has no bearing on the present study because the differences, with respect to RCP values, are extremely slight. However, use of HFC mixing ratios from Velders and the aforementioned halocarbons from WMO have a modest bearing on our companion paper, Mascioli et al. (2012), which projects ΔT to 2060. Future mixing ratios of these species are projected by Velders and WMO to be slightly higher than future mixing ratios in any of the RCP scenarios. Also, radiatively active HFC152a was overlooked in the RCP database.

3.2.2 Anthropogenic radiative forcing: tropospheric aerosols

Figures 2, 3, and 4 detail our treatment of radiative forcing due to anthropogenic tropospheric aerosols, the model input represented by NAA RF_i in Eq. (2). The estimate of NAA RF_i is tied to values of direct RF of mineral dust (Dust), ammonium nitrate (NH_x), fossil fuel organic carbon (OC), fossil fuel black carbon (BC), and biomass burning organic and black carbon (biomass) emissions given by RCP Potsdam (parenthetical

ACPD
12, 23829–23911, 2012

terms refer to Fig. 3). First, we describe how we obtain direct and total RF for sulfate. Then parameters α_{COOL} and α_{HEAT} used to define NAA RF_i are described.

The direct RF for sulfate aerosols ($RF_{SULFATE-DIR}$) given by RCP Potsdam exhibits a steady rise until about 1992, followed by a modest decline until about 2000, then a second peak occurring about around 2010. This time series does not follow the temporal evolution of sulfur emissions (S_{EMISS}) given by either Stern (2006b) or Smith et al. (2011) (Fig. 2a). RCP provides values for S_{EMISS} that are quite similar to those given by Smith et al. (2011), but only on a decadal time scale that does not reflect known, interannual variations (Fig. 2a).

We have formed our own estimate for $RF_{SULFATE-DIR}$, labeled Smith* in Fig. 2b, that is tied to the Smith et al. (2011) estimate of S_{EMISS} and the Stern (2006a) estimate of total RF due to sulfate ($RF_{SULFATE-TOT}$). We have scaled $\mathbf{RF_{SULFATE-TOT}}$ from Stern (2006a) by the ratio of S_{EMISS} from Smith et al. (2011) divided by S_{EMISS} from Stern (2006b). We scale by this ratio because the emissions from Smith et al. (2011) are an update to those from Stern (2006b). The resulting, scaled curve is multiplied by a constant factor, at all times, such that the value of $RF_{SULFATE-DIR}$ in 2005 equals $-0.4\,W\,m^{-2}$, the best estimate of this quantity given in Table 2.12 of IPCC (2007).

The next step in the calculation of NAA RF is to scale $RF_{SULFATE-DIR}$ to $RF_{SULFATE-TOT}$. Our best estimate for $RF_{SULFATE-TOT}$ in year 2005 is $0.96\,W\,m^{-2}$, based on values of $RF_{SULFATE-TOT}$ from Stern (2006a) that extends to 2000, S_{EMISS} from Stern (2006b) that extends to 2000, and S_{EMISS} from Smith et al. (2011) that extends to 2005. A value of 2.4 for α_{COOL} is needed to scale $RF_{SULFATE-DIR}$ in year 2005 (value of $-0.4\,W\,m^{-2}$) to this best estimate of $RF_{SULFATE-TOT}$ in year 2005.

Figure 3 shows time series for total RF of anthropogenic aerosols that cool (Fig. 3a), aerosols that heat (Fig. 3b), and net anthropogenic aerosol RF (Fig. 3c). Figures 3a, b also show components that contribute to the cooling and heating terms, respectively. All time series shown in Fig. 3 are based on direct RF from RCP Potsdam for specific types of aerosols, except for $RF_{SULFATE-DIR}$ (described above). For aerosols that cool, the direct RF terms from RCP are all multiplied by α_{COOL} and these components are

ACPD
12, 23829–23911, 2012

summed to arrive at total RF for aerosols that cool (Fig. 3a). The same procedure is used for aerosols that heat, except a different scaling parameter, α_{HEAT}, is used (Fig. 3b).

While use of two scaling parameters may seem overly simplistic, these parameters capture the essence of the temporal variation of NAA RF in a tractable manner. Chapter 2 of IPCC (2007) establishes that total RF due to aerosols is much larger than direct RF due to aerosols. Our scaling parameters represent the various aerosol feedbacks that occur in the atmosphere, which have a myriad of names such as the first indirect effect, the second indirect effect, cloud albedo effect, the Twomey effect, the Albrecht effect, and the cloud lifetime effect (Fig. 2.10 and Sect. 2.4.1 of IPCC, 2007). Aerosol cooling is dominated by sulfate particles and aerosol heating is dominated by black carbon. The feedbacks that occur for aerosols that cool will likely be dominated by the interactions of sulfate and clouds. The feedbacks that occur for aerosols that heat will be dominated by interactions of black carbon with clouds and snow. While it is possible feedbacks may have changed over time, for example due to a change in the height of power plant smokestacks, movement of meteorological fronts relative to point sources, or a change in the ratio of sulfate to nitrate emission that alters the chemical composition of aerosols that cool, the simplest assumption is that the effect of aerosols on clouds is constant over time. The present state of knowledge regarding aerosol feedbacks is so uncertain that, as noted above, we believe exploration of uncertainty in NAA RF in this highly parameterized manner constitutes an important step forward.

Figure 3 shows time series of total RF from aerosols that cool, total RF from aerosols that heat, and the net affect (NAA RF_i) for specific values of α_{COOL} and α_{HEAT}. We choose year 2005 as a benchmark for NAA RF_i due to the large number of tables and figures in IPCC (2007) that quantify RF of anthropogenic aerosols between 1750 (when NAA RF_i was essentially zero) and 2005 (e.g., Figs. FAQ 2.1, 2.20 and 2.21 as well as Table 2.12 of IPCC, 2007). The value of NAA RF_i at the end of 2005, denoted NAA RF_{2005}, is marked on Fig. 3c. The value for $\alpha_{HEAT} = 2.4$ used in Fig. 3b, which coincidently is the same value used for α_{COOL}, was chosen such that a value of

ACPD
12, 23829–23911, 2012

$-1.0\,W\,m^{-2}$ for NAA RF_{2005} is obtained (Fig. 3c). This matches the IPCC (2007) central value for NAA RF_{2005} (Appendix D).

There is a final important detail regarding the scaling parameters α_{COOL} and α_{HEAT}. There are infinitely many combinations of α_{COOL} and α_{HEAT} that yield the same value of NAA RF_{2005}, as shown in Fig. 4. The red line and black solid lines on this figure denote isopleths of NAA RF_{2005}. The green dashed lines represent the empirical range for NAA RF_{2005}, which we have computed as $-0.4\,W\,m^{-2}$ to $-2.2\,W\,m^{-2}$ based on Table 2.12 of IPCC (2007) (see Appendix D). The lines marked "High Road", "Middle Road", and "Low Road" show three ways that α_{COOL} and α_{HEAT} can be combined to arrive at the same values of NAA RF_{2005}. The region of Fig. 4 bounded by the two limits of the empirical range as well as the High and Low Roads represents our estimate of realistic limits for α_{COOL} and $\alpha_{HEAT.}$

The value for NAA RF_{2005} of $-1.0\,W\,m^{-2}$ (red line, Fig. 4) can result from many combinations of α_{COOL} and α_{HEAT}. However, simulations of climate using Eq. (2) are extremely insensitive to which combination of α_{COOL} and α_{HEAT} is used to arrive at NAA RF_{2005}. In the Supplement, we show simulations for different time series of NAA RF_i, all having NAA $RF_{2005} = -1.0\,W\,m^{-2}$, based on values of α_{COOL} and α_{HEAT} at the intersection of the red line and the "High Road", "Middle Road", and "Low Road" of Fig. 4. Simulations of ΔT_{MDL} are nearly identical. This model behavior occurs because the RF terms, for aerosols that both cool and heat, are all tied to precursor emissions. Precursor emissions of all aerosol types have generally risen over time, driven by population growth, economic productivity, and technology (e.g. Myhre et al., 2001; Stern, 2006b; Smith et al., 2011). Values of S_{EMISS} peaked in 1980 according to Smith et al. (2011) (Fig. 2b), but the deviation of present day emissions from the peak value is too small to discern whether the "High Road", "Middle Road", or "Low Road" analysis provides a better simulation of climate.

The key factor for simulating ΔT from 1900 to present is the value of NAA RF for the modern epoch (represented as NAA RF_{2005} on Fig. 4). When NAA RF_{2005} is towards the upper limit of the empirical range (close to $-0.4\,W\,m^{-2}$), small values of the

ACPD
12, 23829–23911, 2012

sensitivity parameter (i.e. low climate sensitivity) are found following minimization of the Cost Function. In other words, if aerosols have had a modest cooling effect over time, climate feedback must be small. When NAA RF_{2005} is towards the lower limit of the empirical range (close to $-2.2\,W\,m^{-2}$), larger values of the sensitivity parameter result (if aerosols have strongly cooled, climate sensitivity to GHG RF must be high). These parameters cantilever in a similar manner within GCMs (Kiehl, 2007). In Sect. 4, we show this cantilevering has little effect on our primary result: the volcanic cooling term is much more sensitive to whether the AMO term is included in the regression and how AMO is detrended than it is to the value of NAA RF_{2005}.

3.2.3 Atlantic multidecadal oscillation

The Atlantic Multidecadal Oscillation (AMO) is a measure of the variability of SST in the North Atlantic Ocean, generally between the equator and 60° N. Schlesinger and Ramankutty (1994) first described the relation of the modern climate record to the temporal oscillation of SST in the North Atlantic (Fig. 5a, top panel), which tends to vary with a period of 60 to 70 yr. Analysis of oceanic GCM output shows that oscillations of North Atlantic SST reflect variations in the strength of the Atlantic Meridional Overturning Circulation (AMOC), also called the thermohaline circulation (Knight et al., 2005; Stouffer et al., 2006; Zhang et al., 2007, Medhaug and Furevik, 2011). Variations in the deep water formation rate that drives the AMOC primarily affect SST in the North Atlantic in one GCM simulation (Fig. 9 of Stouffer et al., 2006). However, data analysis (Fig. 6 of Dima and Lohmann, 2007) shows expression of variations of AMO throughout the Pacific. Further complicating matters, the relation between AMO and AMOC varies considerably between different ocean GCMs (Medhaug and Furevik, 2011).

There is considerable debate regarding the physical processes that drive variations in the strength of the AMOC, which is described in Sect. 4.3. There is also debate whether the strength of the AMOC has changed monotonically over time due perhaps to rising GHGs (e.g. Box 5.1 of IPCC, 2007; Willis, 2010). Here, we exclusively use an

ACPD
12, 23829–23911, 2012

AMO index detrended for the time period of the regression. Our sole focus is quantification of the impact of AMOC variability on $\Delta T_{\text{VOLCANO}}$.

There are several groups that provide an AMO index. The NOAA AMO is based on SST measurements in the Atlantic from the equator to 70° N, detrended using a linear regression (Enfield et al., 2001). The Royal Netherlands Meteorological Institute (KNMI) provides multiple AMO indices: one based on Atlantic SST from the equator to 60° N detrended using near global SST (60° S to 60° N) (Trenberth and Shea, 2006) and another based on Atlantic SST from 25° N to 60° N detrended using a regression against global temperature (van Oldenborgh et al., 2009). Guan and Nigam (2009) compute an AMO based on principal component analysis of the SST poleward of 20° N. Ting et al. (2009) also report an AMO based on principal component analysis, combined with a low pass filter, using output from six ocean GCMs.

We have examined the impact of most of the AMO indices described above in our model framework (not shown). The most important detail, by far, is how each index was detrended. Below, we present results using three methods for detrending the AMO, performed internally based on SST data from two data centers.

We have obtained SST records from the Hadley Centre (**HadSST3**) and NOAA (Kaplan Extended SST V2, hereafter **KaplanSST2**). In the main paper, we show results using HadSST3. In Supplement, we show that our overall conclusions are unaffected if KaplanSST2 is used rather than HadSST3. At the time of paper submission, HadSST3 extends only to the end of 2006. We have extended HadSST3 to the end of 2011 by concatenating the HadSST2 record, from the start of 2007. There is a slight discontinuity of 0.041 °C for Atlantic SST (equator to 60° N) between the two records at the end of 2006 (HadSST3 is larger than HadSST2). We have added 0.041 °C to the HadSST2 record, so that it joins HadSST3 in a continuous manner.

Figure 5 shows various representations of the AMO from HadSST3. The top panel shows area weighted SST in the Atlantic (equator to 60° N). The bottom three panels show different representations of the AMO, based on how the index has been detrended. Figure 5b shows use of near global SST (60° S to 60° N), as suggested by

ACPD
12, 23829–23911, 2012

Trenberth and Shea (2006). This results in an AMO index with less interannual variability (in an absolute sense) than the other detrending methods and, most importantly, a larger value in the 1900 to 1930 time period. Figure 5c shows use of a linear regression, as described by Enfield et al. (2001). We believe both of these methods for detrending can be critiqued. If the expression of changes in the strength of the AMOC truly extends beyond the North Atlantic, as suggested by Dima and Lohmann (2007), Zhang and Delworth (2007), and Zhang et al. (2007), then use of near-global SST to detrend the AMO removes some of the physical signal. As noted by Trenberth and Shea (2006) as well as Ting et al. (2009), use of a linear regression to detrend the AMO could result in the aliasing of a global warming signal into the resulting index. The intent of the AMO is to arrive at a proxy for variation in a component of the climate system that is independent of anthropogenic RF, which is known to have varied in a non-linear manner over time.

Figure 5d shows a method for obtaining detrended AMO that uses the anthropogenic radiative forcing (AF) of climate. We import, to the model, the record of North Atlantic SST shown in Fig. 5a. For each iteration of the model, prior to computation of regression coefficients, North Atlantic SST is used to form a detrended AMO index by regression against $(1+\gamma)(\text{GHG RF}_i) + (\text{NAA RF}_i)$. Figure 5d shows converged results for GHG RF from RCP 8.5, NAA $\text{RF}_{2005} = -1.0\,\text{W m}^{-2}$ and $\gamma = 0.41$ (i.e. model results shown in Fig. 6d). An AMO index computed in this manner accounts for the fact that growth in background SST over time was non-linear and assumes that variations in AMOC drive interannual variability as well as the 60 to 70 yr oscillation of global SST.

3.2.4 Ocean heat export

As atmospheric levels of GHGs rise, the associated RF perturbation leads to an increase in the temperature of the atmosphere as well as the upper level of the world's oceans (e.g. Church et al., 2011; Schwartz, 2012). There has been a concerted effort within the oceanographic community to define the heat content of the upper 700 m of the global ocean (Ocean Heat Content, or **OHC**), from 1950 onwards, based on

ACPD
12, 23829–23911, 2012

a variety of oceanic temperature measurements and data assimilation products (e.g. Carton and Santorelli, 2008). The ocean also responds to the GHG-induced RF perturbation at a depth below 700 m. However, the time scale for this response is ~500 yr (Schwartz, 2012). Since we are examining rapid variations in ΔT over the past century, we consider only the heat content of the upper 700 m of the world's oceans.

We have based our analysis on the OHC record of Church et al. (2011). Their data span the 1950 to 2009 time period (bottom panel, Fig. 6a). We have conducted a linear least squares fit of their data to determine that OHC rose by 21.3×10^{22} J from 1950 to 2009. To represent this rise in ocean heat within our model, we first convert OHC to heat flux (power), termed Ocean Heat Export (OHE), which represents the flow of energy from the atmosphere to the ocean. Using the surface area of the ocean (3.3×10^{14} m^2) and the time interval of the data record (59 yr or 1.86×10^9 sec), the OHE has averaged 0.347 ± 0.0221 W m^{-2} over the observational period. Schwartz (2012) examined the time constant for the upper 700 m of the ocean to respond to an atmospheric RF perturbation within 5 GCMs and reported a median value of 6.3 yr, which we round to 6 yr for our equation (below) describing Q_{OCEAN}.

We have designed our model to match observed OHE over the 59 yr time period, taking into consideration the 6 yr time constant, which is represented as a 6 yr time lag. We make no attempt to model the ups and downs in the observational record, because the uncertainties in the reconstruction of OHC are the same magnitude as the fluctuations. Furthermore, these fluctuations are often not coherent in time for various OHC estimates (Carton and Santorelli, 2008). The simplest assumption we can make is to consider OHE to be a fixed fraction of the anthropogenic RF perturbation: i.e. the increase in RF of the climate system due to human activity, at any point in time, can either flow into the ocean (where it heats the upper 700 m) or it can remain in the atmosphere (where it heats the land surface and ocean skin). The export of heat from the atmosphere to the ocean is represented by:

$$Q_{\mathrm{OCEAN}\ i} = \Omega[(1+\gamma)\ \mathrm{GHG\ RF}_{i-72} + \mathrm{NAA\ RF}_{i-72}] \quad (4)$$

ACPD
12, 23829–23911, 2012

where

$$\Omega = \frac{\text{OHE}}{\langle (1+\gamma)\text{GHG RF} + \text{NAA RF}\rangle_{\text{TIME INITIAL TO TIME FINAL}}} \quad (5)$$

Physically Eqs. (4) and (5) represent a fixed fraction of the anthropogenic radiative forcing of climate being exported to the upper ocean over time. The index $i - 72$ in Eq. (4) represents the 6 yr (72 month) lag between an atmospheric RF perturbation and heat export to the upper ocean (Schwartz, 2012). The term OHE in Eq. (5) represents the rise in OHC over the period of observation. For the Church et al. (2011) measurement of OHC, Eq. (5) becomes:

$$\Omega = \frac{0.347\ \text{W m}^{-2}}{\langle (1+\gamma)\text{GHG RF} + \text{NAA RF}\rangle_{1944\ \text{to}\ 2003}} \quad (6)$$

The notation $\langle\ \rangle_{1944\ \text{to}\ 2003}$ denotes the mean value of the term enclosed within brackets over the 1944 to 2003 time period. Years 1944 to 2003 are used for the average of anthropogenic RF in the denominator of the expression because of the 6 yr delay between atmospheric perturbation and upper ocean response: OHC was measured by Church et al. (2011) from 1950 to 2009. As γ adjusts to prescribed NAA RF (i.e. as the model iterates), Ω is continuously updated.

The red curve on the bottom panel of Fig. 6a compares the integral over time of the modeled value of Q_{OCEAN} with the Church et al. (2011) estimate of OHC. Clearly the measurement of OHC is matched, on average. The representation of heat flow into the ocean as a fixed fraction of the anthropogenic RF perturbation allows us to simulate Q_{OCEAN} from 1900 to present in a physically consistent manner. Figure 6a shows results for a simulation that excludes terms for AMO, PDO, and IOD. When these terms are included in the regression, modeled OHC is indistinguishable from the red line on the bottom panel of Fig. 6a. For the converged model results shown in Fig. 6, 16 % of the anthropogenic RF perturbation has gone into the upper 700 m of the ocean (i.e. $\Omega = 0.16$).

ACPD
12, 23829–23911, 2012

Gouretski and Reseghetti (2010) provide a different estimate for OHC, spanning the 1993 to 2008 time period, which is much larger than the estimate of Church et al. (2011). The value of OHC from Gouretski and Reseghetti (2010) implies 36 % of the anthropogenic RF perturbation has flowed into the upper ocean. Use of the Gouretski and Reseghetti (2010) value of OHC has no bearing on the results of this paper; γ adjusts to match ΔT and all of our conclusions involving $\Delta T_{\mathrm{VOLCANO}}$ are insensitive to OHC. On the other hand, future temperature is sensitive to γ, because NAA RF will decline over time (i.e. this feedback parameter and the resulting climate sensitivity will control ΔT at the time atmospheric CO_2 doubles). We show model results using the Gouretski and Reseghetti (2010) value for OHC in our companion paper, which is focused on future ΔT.

4 Results

4.1 Global surface temperature

Figure 6 compares monthly, global temperature anomaly (ΔT) reported by CRU4, from 1900 to the end of 2010, with the modeled value of ΔT (top panel of each "ladder plot"). Figure 6a shows a regression that includes proxies for volcanoes, TSI, humans (GHG RF and NAA RF), and ENSO. The various rungs of the ladder show the product of the regression coefficient and the proxy. The red line in the top rung of Fig. 6a is the sum of the four lines shown below, plus the constant term (not shown). The $\sim$1 °C rise in temperature over the 110 yr period is attributed to anthropogenic radiative forcing of climate ("Human" panel, Fig. 6a). All of the simulations shown in Fig. 6 use GHG RF from RCP 8.5 as well as the time series for NAA RF shown in Fig. 3c: i.e. NAA $\mathrm{RF}_{2005} = -1.0\,\mathrm{W\,m^{-2}}$ found using values of α_{COOL} and α_{HEAT} along the Middle Road of Fig. 4. High frequency variations superimposed on the long term record are primarily attributed to the El Niño-Southern Oscillation. Volcanoes account for short term decreases in ΔT, with Pinatubo associated with a 0.33 °C drop in global mean

ACPD
12, 23829–23911, 2012

surface temperature. Variations in total solar irradiance lead to an 11 yr cycle in ΔT: note the y-axis for the solar rung of Fig. 6a has a different scale than the other rungs, chosen to accentuate the solar cycle.

The cooling attributed to Pinatubo shown in Fig. 6a is quite similar to results of Lean and Rind (2008). They reported a maximum ~0.3 °C cooling due to Pinatubo based on a MLR analysis of an earlier version of the CRU global surface temperature record.

Figure 6b, c and d show comparisons similar to Fig. 6a, except proxies for the AMO, PDO, and IOD have been added to the regression. The comparison of measured and modeled OHC, as noted above, is only shown once because this plot is nearly identical for all of the simulations. Figure 6b considers the AMO from HadSST3 (abbreviated Had3) detrended using near-global SST ($AMO_{Had3\ SST}$). Figure 6c shows results for Had3 AMO detrended using a linear regression ($AMO_{Had3\ Lin}$) and Fig. 6d shows Had3 AMO detrended using anthropogenic radiative forcing of climate ($AMO_{Had3\ AF}$). The effect of the Pacific Decadal Oscillation and Indian Ocean Dipole on global climate is minimal. These proxies are not discussed further even though for completeness we continue to use the PDO and IOD in other regressions.

The panels labeled Atlantic in Fig. 6 suggest, depending on how the AMO is detrended, variations in the strength of the AMOC may have an impact on global climate that is larger in magnitude than ENSO. There is steady improvement in the ability to simulate global surface ΔT reported by CRU4 as the AMO is added to the model (Fig. 6b versus Fig. 6a), then as the method for detrending the AMO is changed from SST to LIN (Fig. 6c versus Fig. 6b), and from LIN to AF (Fig. 6d versus Fig. 6c). The top panel of each ladder plot includes the numerical value of reduced chi-squared, defined as:

$$\chi^2 = \frac{1}{(N_{\mathrm{MONTHS}} - N_{\mathrm{FITTING\ PARAMETERS}} - 1)} \sum_{i=1}^{N_{\mathrm{MONTHS}}} \frac{1}{\sigma^2_{\mathrm{OBS}\ i}} (\Delta T_{\mathrm{OBS}\ i} - \Delta T_{\mathrm{MDL}\ i})^2 \qquad (7)$$

where $N_{\mathrm{FITTING\ PARAMETERS}}$ equals 5 for Fig. 6a (4 regression coefficients plus γ) and equals 8 for Fig. 6b, 6c and 6d (3 additional regression coefficients). Physically, a value

ACPD
12, 23829–23911, 2012

of $\chi^2 \leq 2$ indicates that the model agrees with the observations, within the measured uncertainty. All four simulations meet this criterion. The drop in the value of χ^2, from Fig. 6a to Fig. 6d, quantifies the steady improvement in the ability to simulate ΔT as the AMO is first considered and then as its treatment is varied. The increase in the amplitude of the green lines in the Atlantic rung, from Fig. 6b to Fig. 6d, demonstrates that increased importance of the AMO is responsible for the steady decline in χ^2.

Figure 1 of Lean and Rind (2008) includes notation for the pre-WWI and WWII time periods, during which global climate has been traditionally difficult to simulate. The $AMO_{Had3\ AF}$ model (Figs. 6d) is able to simulate pre-WWI and WWII particularly well, due in part to changes in the SST record during these periods of time compared to the CRU3 record (Thompson et al., 2008) but mainly due to significant cooling during pre-WWI and large heating during WWII due to variations in the strength of the AMOC that are picked up by this regression. The $AMO_{Had3\ AF}$ regression simulates pre-WWI cooling and WWII warming of the CRU4 land temperature anomaly particularly well (Fig. 7d), supporting the possibility that variations in the strength of the AMOC have truly exerted influence on global climate and also that the $AMO_{Had3\ AF}$ index is a valid proxy for the AMOC. The $AMO_{Had3\ Lin}$ and $AMO_{Had3\ AF}$ models yield stronger contributions of AMOC to global ΔT than the $AMO_{Had3\ SST}$ simulation, throughout the 110 yr period, because for the 1900 to 1930 portion of the record the AMO is deemed to be strongly negative when detrended using either LIN or AF (Fig. 5).

As the influence of the AMO on global climate becomes more prominent, the volcanic regression coefficient declines (volcanic rungs, Fig. 6). The maximum cooling attributed to Pinatubo is 0.33 °C without consideration of the AMO. Pinatubo cooling drops to 0.15 °C for both the $AMO_{Had3\ Lin}$ and $AMO_{Had3\ AF}$ simulations (numerical values given in Table 1). Global ΔT after the eruption of Pinatubo is simulated just as well in Fig. 6c and d as in Fig. 6a: in Fig. 6c and d, the model attributes a portion of the observed decline in temperature to the AMO rather than to SOD.

A factor of 2 reduction in the cooling attributed to Pinatubo, upon consideration of the AMO, challenges conventional wisdom. Many prior studies have accounted for

ACPD
12, 23829–23911, 2012

ENSO-related influence on temperature for quantification of volcanic cooling. None have considered an AMOC-related influence, which could potentially be larger in magnitude than the ENSO influence (e.g. panels labeled El Nino and Atlantic in Fig. 6). A possible criticism of the analysis presented in Fig. 6 is that, since the SST record contributes to both the AMO (based on SST in the North Atlantic) and global temperature (combination of land surface temperature and SST), there could be an element of "circularity" to the analysis. We examine next the land surface temperature record, for which there is no possibility of circularity.

4.2 Land surface temperature

Since the determination of ΔT over land is completely independent of SST, the presence of the 60 to 70 yr period oscillation in the land temperature record is strong observational evidence that the AMOC has an effect on global climate. Figure 7 is identical to Fig. 6, except Fig. 7 is based on analysis of the global land surface temperature anomaly (ΔT_{LAND}) from CRU4. Greater volcanic cooling over land is readily apparent. Large, high frequency variations in ΔT_{LAND} are also apparent, resulting in higher values of χ^2 compared to the simulation of global temperature. There is a steady improvement in the ability to simulate ΔT_{LAND} as the AMO is first added to the model (Fig. 7b versus Fig. 7a), then as the method used to detrend the AMO is changed from SST to either LIN (Fig. 7c) or AF (Fig. 7d). A maximum cooling of 0.55 °C is associated with Pinatubo when the AMO is neglected in the regression, consistent with the commonly accepted value.

The computed cooling due to Pinatubo falls to 0.29 °C and 0.35 °C, respectively, when $\mathrm{AMO}_{\mathrm{Had3\ Lin}}$ or $\mathrm{AMO}_{\mathrm{Had3\ AF}}$ are used in the regression. As apparent in the top panels of Figs. 7c and 7d, the modeled ΔT_{LAND} drops by ~0.5 °C at the time of peak SOD following the eruption of Pinatubo. However, when either $\mathrm{AMO}_{\mathrm{Had3\ Lin}}$ or $\mathrm{AMO}_{\mathrm{Had3\ AF}}$ is used in the regression, a significant portion of this observed cooling is attributed to the AMOC and not Pinatubo. The CRU4 climate record indicates a perturbation to ΔT_{LAND} similar to that reported by Hansen et al. (1993) and Lacis and

ACPD
12, 23829–23911, 2012

Mishchenko (1995): our interpretation of the cause of a portion of this cooling is all that differs.

A literal interpretation of the χ^2 values given in the top panels of Fig. 7 could lead one to conclude that only the simulations shown in panels Fig. 7c and Fig. 7d represent a model consistent with observations, to within the uncertainty of measurement. We are not suggesting such a literal interpretation because values of χ^2 are affected by the high frequency noise of the data record, as well perhaps the invariably subjective nature of specification of measurement uncertainty (i.e. our analysis of the BEG land temperature record never achieves anywhere close to $\chi^2 = 2$ because of the vanishingly small uncertainties associated with this data record; see Table 2). For the CRU4 land record, when the AMO is neglected (Fig. 7a), ΔT_{OBS} exhibits a sharper increase since the mid-1990s than represented in the model. Simulations that include the AMO are able to represent ΔT_{OBS} since the mid-1990s better than the simple model, suggesting that a change in the AMO might be responsible for part of the recent temperature rise. And, similar to the simulation of global ΔT, variations of ΔT_{LAND} at the time of pre-WWI and WWII are represented much better when the AMO is included in the regression. Regression of ΔT_{LAND} also results in consistently larger values of γ compared to the simulation of global ΔT, indicative of more rapid warming over land than ocean.

4.3 Cause and effect

The reduction of $\Delta T_{\mathrm{PINATUBO}}$ upon consideration of the AMO begs the question regarding cause and effect of the variations in the strength of the AMOC. Kuhlbrodt et al. (2007) have written a detailed overview of the AMOC. There are two distinctly different theories emerging regarding AMOC variability: the ocean salinity/sea ice theory and the atmospheric aerosol/volcano theory.

Dima and Lohmann (2007) suggest variations in the strength of the AMOC are caused by the export of sea ice through the Fram Strait, driven by atmosphere-ocean patterns of sea level pressure throughout the Arctic. Temporal variations in sea ice export affect salinity and hence the rate of deep water formation. The freshening of

ACPD
12, 23829–23911, 2012

the North Atlantic due to larger flux of sea ice inhibits deep water formation, causing a cooling (negative AMO). Their reconstruction of Fram Strait sea ice export exhibits temporal variations (i.e. a small amplitude 60 to 70 yr period oscillation, superimposed on a high amplitude interannual oscillation) quite similar to North Altantic SST. Zhang et al. (2007) have suggested the AMOC drives multidecadal variability of temperature throughout the Northern Hemisphere. Delworth and Zeng (2012) present results of a 4000 yr GCM simulation that exhibits internal variability of the AMOC, due to propagation of salinity anomalies, that lead to 0.1 to 0.3 °C hemispheric-scale temperature anomalies (i.e. the same magnitude as the green curves in Figs. 6c, d and 7c, d). Meehl et al. (2011) recently presented a five-member ensemble GCM simulation of future climate that shows ~0.5 °C variations in global temperature they identify as being due internally generated, decadal timescale variability in OHC. The decadal time scale variability for future global temperature shown in Fig. 1a of Meehl et al. (2011) looks remarkably similar to the decadal time scale variability shown in the Atlantic rungs of our Figs. 6c, d and 7c, d.

On the other hand, a number of recent studies have focused on AMOC variability driven by tropospheric aerosols and volcanoes. Church et al. (2005) suggested the eruption of Pinatubo resulted in rapid reductions in both OHC and global mean sea level. Stenchikov et al. (2009) present a GCM simulation that showed volcanic cooling could strengthen the AMOC. Zanchettin et al. (2012) suggested the strengthening of the AMOC would maximize about 10 yr after a major volcanic eruption. Murphy et al. (2009) point to a relation between enhanced volcanic aerosol and a brief cessation of flow of energy into the ocean, based on an 8 yr linear fit smoothing of the derivative, with respect to time, of OHC reported by Domingues et al. (2008). Booth et al. (2012) implicate an optical depth anomaly driven by temporal variation of tropospheric aerosols (pollution) and stratospheric sulfate (volcanoes) as a primary driver of SST variability in the North Atlantic.

However, the linkages between volcanic eruptions, AMOC, and OHC are not well established. Iwi et al. (2012) do not find strong evidence for an effect of Pinatubo on

ACPD
12, 23829–23911, 2012

the strength of the AMOC and Carton and Santorelli (2008) state that their analysis of OHC does not seem to reflect an impact from the eruption of Pinatubo. As shown in the Supplement, the derivative of OHC from Church et al. (2011), an update to the record of Domingues et al. (2008), bears no relation to SOD (hence, the conclusion of Murphy et al. seems highly dependent on which OHC record is used, and possibly how the data are smoothed). There is extensive literature on this subject, nearly entirely focused on the debate of whether or not major volcanic eruptions affect OHC and the strength of the AMOC. Our study seems to be the first to suggest that variations in the strength of the AMOC may have compromised prior estimates of volcanic cooling.

Figure 8 examines time series of SOD and the $AMO_{Had3\ AF}$ in an attempt to probe cause and effect. Data obtained after perturbations to SOD from the four major eruptions since 1900, Santa María, Agung, El Chichón, and Pinatubo, are indicated using specific colors. Figure 8 shows that the AMO was in a negative phase (i.e. North Atlantic SST tended to be lower than average) at the time SOD was perturbed by the eruptions of Santa María, El Chichón, and Pinatubo. The $AMO_{Had3\ AF}$ was neutral at the time of the Agung eruption. As shown in Supplement, this plot looks similar for $AMO_{Had3\ SST}$ and $AMD_{Had3\ Lin}$, except the AMO is much closer to neutral after the eruption of Santa María when detrended using SST.

The middle bottom panel of Fig. 8c shows a scatter plot of SOD versus $AMO_{Had3\ AF}$. This is purely a combination of the SOD record as reported by Sato et al. (1993) and the AMO signal deduced from HadSST3. Following the eruptions of Santa María, Agung, El Chichón, and Pinatubo, there were 176 months when SOD exceeded 0.01, which we consider to be the volcanic threshold based on visual inspection of the SOD record. For 142 of these months, $AMO_{Had3\ AF}$ was negative. The left panel of Fig. 8c shows a similar scatter plot, except here the SOD signal has been moved earlier in time by 6 months. Individual data points move because SOD is now aligned with a different value of $AMO_{Had3\ AF}$. Remarkably, the numerical breakdown is unaltered: 6 months prior to volcanic perturbation of SOD, the AMO tended to be in a negative phase 80 % of the time! We have to slide SOD backwards in time, by about 2 yr, for there to be a 50:50

ACPD
12, 23829–23911, 2012

split between negative and positive phases of the AMO in the scatter plot. If the SOD signal is moved in the opposite direction, later in time, the AMO tends to be slightly less negative (right panel, Fig. 8c). These scatter plots suggest that variations in North Atlantic SST, as reflected in the AMO, occurred prior to the volcanic perturbation to SOD. Also, there is no suggestion that when SOD achieves a local maximum (i.e. peak volcanic perturbation), the AMO is at a local minimum either coincident in time with peak SOD (as suggested by the GCM of Booth et al., 2012), ~2 to 3 yr after peak SOD (as suggested by the GCM of Stenchikov et al., 2009), or ~10 yr after peak SOD (as suggested by the GCM of Zanchettin et al., 2012) (see Supplement).

It is an enormous challenge to define an AMO index absent volcanic influence. Our empirical examination of AMO from HadSST3 (Fig. 8) and the OHC record (Supplement) does not present evidence for a volcanic signature. If a future consensus emerges that major volcanic eruptions truly do impose a large imprint on the AMO, such that the indices used in our analysis are flawed (i.e. do not represent AMOC) either at the time SOD was elevated or soon (~6 months) after each eruption, then clearly our results are invalid. We conclude by noting three crucial points: (1) the regression coefficient for the AMO signal is driven by data collected at times other than the SOD perturbation, which we have confirmed by removing data collected during times of peak SOD and repeating the analysis; (2) if there is a 2 or 10 yr delay in the imprint of SOD on AMO, as suggested by Stenchikov et al. (2009) and Zanchettin et al. (2012), respectively, then our analysis should be valid because the AMO at the time of SOD perturbation would not be strongly affected by the volcano; (3) if the 60 to 70 yr periodicity in the AMO is truly caused by a tropospheric aerosol optical depth anomaly, as suggested by Booth et al. (2012), then our conclusion that volcanic cooling has been over estimated is still valid, because this conclusion is dependent only on the notion that North Atlantic SST variability reflects an external forcing of the climate system with global influence that has been overlooked in prior empirical estimates of volcanic cooling, regardless of physical origin (provided of course that the origin is not volcanic).

ACPD
12, 23829–23911, 2012

4.4 Robustness of reduced impact of volcanoes upon consideration of AMO

Table 1 and Figs. 9 and 10 are designed to assess the robustness of our suggestion that variations in the strength of the AMOC may have compromised prior estimates of volcanic cooling. Table 1 shows values of the maximum cooling attributed to Pinatubo, denoted $\Delta T_{\text{PINATUBO}}$, found using all available long-term climate records (Sect. 2). Table 2 shows minimum values of χ^2 found from each regression. Numerical values are based on the product of 0.15 (maximum SOD after Pinatubo) and the SOD regression coefficient. The reduction of $\Delta T_{\text{PINATUBO}}$ upon consideration of AMO in the regression as well as the dependence of $\Delta T_{\text{PINATUBO}}$ on the method used to detrend the AMO are apparent for all of the long-term climate records.

The sensitivity of volcanic cooling to anthropogenic aerosols is now examined. So far we have only shown model results for NAA $\text{RF}_{2005} = -1.0\,\text{W m}^{-2}$, the IPCC (2007) best estimate of NAA RF_{2005}. There is considerable uncertainty in NAA RF_{2005} (Appendix D). Figure 9a and b show how the sensitivity parameter γ (Eq. 2) varies as a function of NAA RF_{2005}, for values of α_{COOL} and α_{HEAT} along the middle road of Fig. 4. End points of the line segments denote the empirical range for NAA RF_{2005} from IPCC (2007) (Appendix D). Model results for NAA $\text{RF}_{2005} = -1.0\,\text{W m}^{-2}$ are included, as well as the range of NAA RF_{2005} represented in GCMs described by Kiehl (2007). Figure 9a and b show the cantilevering of γ and NAA RF_{2005} that was described by Kiehl (2007). Most importantly, the relation of these two model parameters is insensitive to AMO. Our model indicates a more compact relation between these terms than found within the GCMs examined by Kiehl (2007), probably because all of our simulations are constrained to match the same value of OHC. The sensitivity of γ to OHC is explored in Mascioli et al. (2012).

Figure 9c and d show the sensitivity of $\Delta T_{\text{PINATUBO}}$ (same quantity reported in Table 1) to NAA RF_{2005}. The computed value of $\Delta T_{\text{PINATUBO}}$ is moderately sensitive to NAA RF_{2005}. As the cooling attributed to tropospheric aerosols rises (i.e. as NAA RF_{2005} approaches $-2.2\,\text{W m}^{-2}$), cooling attributed to Pinatubo falls. Figure 9c

ACPD
12, 23829–23911, 2012

and d also show the dependence of $\Delta T_{\text{PINATUBO}}$ on AMO. Cooling attributed to Pinatubo depends strongly on whether the AMO is considered as well as the method used to detrend the index, for all values of NAA RF.

Wigley et al. (2005a) allowed for a lag of the ENSO index, of 6 to 7 months, when removing the influence of ENSO on the temperature record. Lean and Rind (2008) lagged ENSO by 4 months. A lag of ENSO by 4 to 7 months has a minor effect on our simulations. For model results shown in Fig. 6d, we obtain the lowest value of χ^2, 0.60, using a lag of 4 months. The value of C_1 changes from –1.036 °C/optical depth (Fig. 6d) to –1.201 °C/optical depth when ENSO is lagged by 4 months. This a small difference in volcanic cooling compared to whether or not AMO is included in the regression.

Figure 10 is complementary to Table 1 and Fig. 9. Figure 10 shows $\Delta T_{\text{VOLCANO}}$ as a function of SOD for simulations of six long-term climate records. Results are shown for no AMO in the regression and for $\text{AMO}_{\text{Had3 SST}}$ and $\text{AMO}_{\text{Had3 Lin}}$ (results for $\text{AMO}_{\text{Had3 AF}}$ are not shown because these lines are nearly indistinguishable from $\text{AMO}_{\text{Had3 Lin}}$). The maximum perturbation to SOD following the 4 major eruptions in the past century is indicated by the colored arrows. At maximum SOD, we show uncertainties for $\Delta T_{\text{VOLCANO}}$ (which can also be considered $\Delta T_{\text{PINATUBO}}$, since maximum SOD is due to Pinatubo). The thick error bar represents the 1-sigma statistical uncertainty in the SOD regression coefficient due to consideration of $\sigma_{\text{OBS}\ i}$ (Appendix C). We have also computed sensitivity of the SOD regression coefficient to uncertainty in NAA RF_{2005} (Fig. 9) and combined this value using root sum of squares with the statistical uncertainty to find the total uncertainty, shown by the thin, light blue error bars.

Five of the six long-term climate records considered in Fig. 10 show a similar pattern: after the AMO detrended using SST is introduced into the regression, $\Delta T_{\text{VOLCANO}}$ falls. If detrending of the AMO using either LIN (shown) or AF (not shown but similar to LIN) is the correct way to represent the impact of variations in the strength of the AMOC on global temperature, then inferred $\Delta T_{\text{VOLCANO}}$ is about a factor of 2 smaller than has been previously reported. The GISS Land record for ΔT is the outlier: this data record shows much less sensitivity to either consideration of the AMO or the method used to

ACPD
12, 23829–23911, 2012

detrend the AMO. With the exception of GISS Land, there is no overlap between the uncertainties for a model that does not consider AMO with the uncertainties for a model that uses $AMO_{Had3\ LIN}$. Based on Table 1 as well as Figs. 9 and 10, we conclude our suggestion that variations in the strength of the AMOC may have compromised prior estimates of volcanic cooling is a robust result of the MLR analysis.

4.5 Atmospheric temperature

We now turn our attention to the record of lower tropospheric temperature provided by MSU. Hansen et al. (1993), Lacis and Mischenko (1995), and Soden et al. (2002), often cited in reference to the 0.5 °C cooling due to Pinatubo, also examined lower tropospheric temperature from MSU.

Figure 11 shows an analysis of the global lower tropospheric ΔT from MSU, which covers the time period December 1978 to December 2011. Figure 12 is identical to Fig. 11, except for land. We use the same approach, MLR, as applied to the 110 yr record of surface ΔT. The results in Figs. 11 and 12 must be interpreted with caution because the 32 yr period covers only 2 volcanoes, less than 3 full solar cycles, and less than a full cycle of AMO (which has a period of 60 to 70 yr). Nonetheless, as seen for simulations of surface ΔT, the cooling attributed to volcanoes falls as the AMO is introduced into the regression and there is a modest dependence of $\Delta T_{VOLCANO}$ on the method used to detrend the AMO. It has long been known that the cooling associated with the eruption of El Chichón in spring 1982 was moderated by ENSO warming (e.g. Thompson, 1995; Wigley et al., 2005a). Warming due to ENSO at the time of peak SOD due to El Chichón is picked up well by our regression model. Maximum cooling due to Pinatubo is found to be 0.41 °C globally and 0.50 °C over land when the AMO is not included in the regression. These numerical values agree with the results of Hansen et al. (1993), Lacis and Mischenko (1995), and Soden et al. (2002).

Our estimates of the cooling attributed to Pinatubo drop to 0.31 °C (global) and 0.36 °C (land) when $AMO_{Had3\ AF}$ is used in the regression. Model parameters $\Delta T_{VOLCANO}$ and γ are both larger for land than global, consistent with the notion that

ACPD
12, 23829–23911, 2012

lower tropospheric temperature is more sensitive to radiative perturbations over land than over ocean. These estimates for the cooling attributed to Pinatubo are considerably smaller than the 0.5 °C values discussed by Hansen et al. (1993), Lacis and Mischenko (1995), and Soden et al. (2002). As apparent in our figures, the atmosphere did indeed cool by ∼0.5 °C at the time of peak SOD following the eruption of Pinatubo. But when $AMO_{Had3\ AF}$ is used in the regression, a significant portion of this cooling is attributed to the AMOC and not Pinatubo.

The quality of fit indicated by numerical values of χ^2 improves considerably as the AMO is added to the regression, and moderately as the method used to detrend AMO is varied. However, none of the regressions approach $\chi^2 = 2$. This is likely due to a combination of small values for σ_{OBS} of MSU (error bars for MSU ΔT shown in Figs. 11 and 12 are much smaller than error bars for CRU4 ΔT shown in Figs. 6 and 7) as well as climate variability. For instance, the cloud height anomaly reported by Davies and Molloy (2012) shows a sharp drop in late 2007/early 2008 (see their Fig. 1) that is well aligned with a drop in MSU ΔT: a decline in cloud height, all else being equal, should cause lower tropospheric cooling. This feature is not picked up by the regression because the sensitivity parameter is held constant. Given the nature of lower tropospheric temperature, this quantity will be more sensitive to short term forcings, such as cloud height anomaly, than global surface temperature.

Nonetheless, consideration of the AMO in the regression improves the simulation of MSU ΔT. Many of the short-term fluctuations present in the MSU temperature record are picked up by the model shown in Figs. 11d and 12d ($AMO_{Had3\ AF}$) and are not apparent in the model shown in Figs. 11a and 12a (no AMO). Analysis of the MSU record increases our confidence that the AMO is a realistic proxy for the effect of variations in the strength of the AMOC on global climate. The numerical values of $\Delta T_{PINATUBO}$ given above support our suggestion that volcanic cooling may have been over estimated, by about a factor of 2, in prior studies due to neglect of the AMOC.

ACPD
12, 23829–23911, 2012

5 Discussion

We have presented an analysis of the climate record, using multiple linear regression, that suggests ocean circulation may be responsible for a portion of the ∼0.3 to 0.5 °C cooling that followed the eruption of Mount Pinatubo. If further scientific study establishes that the AMOC did indeed perturb global climate in the early 1990s, then a recalibration of the use of Mount Pinatubo as a proxy for geo-engineering of climate may be needed. Here, we focus on the physical understanding of volcanic cooling and the implications of our study for geo-engineering of climate.

5.1 Physical understanding of volcanic cooling

Many studies of volcanic cooling, including Hansen et al. (1993), Lacis and Mischenko (1995), Soden et al. (2002), Forster and Collins (2004), Wigley et al. (2005a), and Stenchikov et al. (2009), use GCMs far more sophisticated than our simple regression analysis. This section is motivated by the fact, illustrated in Fig. TS.23 of IPCC (2007), that most GCMs overestimate the observed perturbation to global mean surface temperature following the eruption of Mount Pinatubo. The thick red line of Fig. TS.23 shows modeled ΔT from many GCMs, which declines much more than observed ΔT following the eruption of Pinatubo.

We begin by examining the perturbation to Earth's solar (shortwave, SW) and thermal (longwave, LW) radiation budget after Pinatubo. Figure 13 shows ERBE observations for the tropics (20° S to 20° N) and 60° S to 60° N. The tropical panel is nearly identical to Fig. 2 of Trenberth and Dai (2007) and the 60° S to 60° N panel is similar to Fig. 1 of Soden et al. (2002). The eruption of Mount Pinatubo led to a dramatic increase in stratospheric sulfate aerosol loading, causing a large rise in the reflection of solar radiation due to the optical properties of sulfuric acid droplets. The effect of volcanic aerosols was clearly seen in surface solar radiation measurements: after the eruption of Pinatubo, the amount of direct SW radiation hitting the surface fell dramatically, the amount of diffuse SW radiation rose in tandem, resulting in a net maximum ∼6 $W m^{-2}$

ACPD
12, 23829–23911, 2012

drop in total SW radiation reaching the surface at Mauna Loa (Dutton and Bodhaine, 2001). However, volcanically induced aerosols also trap thermal radiation. This is less well documented, particularly at the surface. In the tropics, the ERBE record shows that increased reflection of solar radiation following Pinatubo dominates trapping of thermal radiation, resulting in a peak net perturbation to the radiative budget of $\sim$6.0 W m^{-2}. In contrast, for 60° S to 60° N, the solar and thermal terms are close in magnitude resulting in a peak net perturbation to the radiative budget of less than 3.0 W m^{-2}. Nearly all of this perturbation occurs in the tropics: the net radiative effect of Pinatubo poleward of 20° latitude was small in the Northern Hemisphere and essentially zero in the Southern Hemisphere (see Supplement). Our analysis of ERBE data is in good agreement with Harries and Futyan (2006).

Soden et al. (2002) showed that the GFDL GCM was able to simulate, remarkably well, the perturbation to the solar and thermal radiation fields induced by Pinatubo over the 60° S to 60° N region. The ERBE measurements represent the radiative perturbation at the top of the atmosphere, not the tropopause. Matching ERBE is a necessary but not sufficient condition for accurate simulation of the affect of volcanic aerosols on climate. We discuss the need for accurate simulation of the stratospheric response below. Also, as discussed in Sect. 1, Soden et al. (2002) (and other studies) require a significant positive feedback due to changes in tropospheric H_2O to match the MSU lower troposphere temperature anomaly. They state "without the strong positive feedback from water vapor, the model is unable to reproduce the observed cooling". Soden et al. (2002) show quite favorable comparisons of modeled and measured upper tropospheric H_2O that support the notion that a strong, positive water vapor feedback did occur. Forster and Collins (2004) reached similar conclusions as Soden et al. (2002), also based on GCM simulations. Both studies accounted for the effect of ENSO on ΔT and neither study considered the possibility that variations in the strength of the AMOC could have affected ΔT.

Wigley et al. (2005a) present an analysis of the major volcanic eruptions since 1900, using the National Center for Atmospheric Research (NCAR)/US Department

ACPD
12, 23829–23911, 2012

of Energy (DOE) GCM. They provide extensive discussion of the effect of ENSO on the inference of volcanic cooling, but do not discuss possible effects due to variations in the strength of the AMOC. Wigley et al. (2005a) concluded maximum global surface cooling associated with Pinatubo was $0.61 \pm 0.1\,^{\circ}\mathrm{C}$, consistent with a climate sensitivity of $3.03\,^{\circ}\mathrm{C}$ (range 1.79 to $5.21\,^{\circ}\mathrm{C}$). Their climate sensitivity refers to equilibrium warming for a doubling of CO_2 ($\Delta T_{2\times CO_2}$). In our notation, $\Delta T_{2\times CO_2}$ is expressed as:

$$\Delta T_{2\times CO_2} = \lambda(1 + \gamma)\, 5.35\, \ln(2)\ \mathrm{W\,m^{-2}} \tag{8}$$

where the RF due to CO_2, $5.35 \ln(CO_2^{FINAL}/CO_2^{INITAL})\ \mathrm{W\,m^{-2}}$, is the IPCC (2007) expression originally published by Myhre et al. (1998). Using values for γ from Figs. 6d and 7d, our model would imply $\Delta T_{2\times CO_2}$ of $1.57\,^{\circ}\mathrm{C}$ for global temperature and $2.03\,^{\circ}\mathrm{C}$ for surface land temperature. Our global value is above the lower limit of IPCC (2007) and just below the lower limit of Wigley et al. (2005a). The land value is within the Wigley et al. (2005a) range, although Wigley focused exclusively on global surface temperature. The model value of γ, which drives $\Delta T_{2\times CO_2}$, is highly dependent on both NAA RF (Fig. 9) and the treatment of OHE (Mascioli et al., 2012). Wigley et al. (2005a) do not discuss the impact of uncertainties in NAA RF on climate sensitivity. Our model, run for NAA $RF_{2005} = -2.2\,\mathrm{W\,m^{-2}}$ along the "Middle Road" of Fig. 4 and constrained to match the OHC measurement of Gouretski and Reseghetti (2010), for $AMO_{Had3\,AF}$, yields $\Delta T_{PINATUBO} = -0.13\,^{\circ}\mathrm{C}$ and $\gamma = 1.02$, implying $\Delta T_{2\times CO_2} = 3.7\,^{\circ}\mathrm{C}$. The relation between γ, NAA RF, and OHE is further quantified by Mascioli et al. (2012). We include these numerical details to emphasize our MLR results are well within the range of previously published GCM results.

Douglass and Knox (2005) conducted a regression analysis of MSU lower tropospheric temperature measurements and concluded the atmosphere exhibited a negative feedback following the eruption of Pinatubo. This paper has been discussed in a series of published comments and replies following initial publication. We stress our model always requires positive feedback, as reflected in values of γ always exceeding zero, and hence our findings are inconsistent with those of Douglass and Knox (2005).

ACPD
12, 23829–23911, 2012

If NAA RF_{2005} approaches the upper limit of $-0.4\,W\,m^{-2}$, γ becomes small, but never drops below 0 (Fig. 9).

Stenchikov et al. (2009) state "In this study, Pinatubo aerosols globally decrease the incoming net radiative flux at the top of the atmosphere by about $3\,W\,m^{-2}$ at maximum that is consistent with most of the IPCC-AR4 models . . . this radiative perturbation dominated all other forcings for at least two years". The radiative perturbation of Pinatubo was enormous for the tropics (Fig. 13a). The radiative perturbation is much smaller when examined over the 60° S to 60° N region. Here, the SW perturbation peaks at $3.7\,W\,m^{-2}$, which occurs 2 months after the eruption, and averages $1.7\,W\,m^{-2}$ for the first 2 yr. ERBE shows a drop in outgoing LW radiation that counteracts the increased reflection of SW radiation. The net perturbation (LW-SW) at the top of the atmosphere, from 60° S to 60° N, peaks at $-2.5\,W\,m^{-2}$ about 2 months after the eruption and has a mean value of $-0.67\,W\,m^{-2}$ for the first 2 yr. The GCM simulations of Stenchikov et al. (2009) represent this LW trapping of heat by volcanic aerosol. Within their model, LW trapping tends to heat the lower stratosphere, reinforcing the notion that correct modeling of the stratospheric response and the downward influence on the troposphere is vital.

Had the maximum ERBE net, near-global perturbation of $-2.5\,W\,m^{-2}$ (measured at top of the atmosphere) acted entirely on the tropopause and below, a simple (but erroneous) analysis suggests that a major drop in globally averaged surface temperature should result. A rough estimate of the impact can be obtained using the expression $\lambda(1+\gamma)\Delta RF$. When evaluated for $\gamma = 0.41$ (Fig. 6d) and $\Delta RF = -2.5\,W\,m^{-2}$, this results in an estimate for global surface cooling of 1 °C. Of course, cooling of this magnitude would not actually occur due to the thermal inertia of the ocean (Wigley et al., 2005b). Calculation of the actual response requires use of an atmosphere ocean GCM that provides a realistic representation of the thermal inertia of various components of the climate system, as well as the stratospheric response.

We now turn to the stratosphere. The eruption of Pinatubo induced major changes in stratospheric dynamics and temperature. Tropical stratospheric temperature rose and

ACPD
12, 23829–23911, 2012

tropical upwelling increased (e.g. Kinne et al., 1992). Stratospheric ozone fell, first in the tropics (Schoeberl et al., 1993) and then at mid-latitudes (Kinnison et al., 1994). Quantitative understanding of the amount of stratospheric ozone depletion following the eruption of Pinatubo requires realistic representation of the dynamical change (Kinnison et al., 1994) as well as accounting for the influence of both natural and anthropogenic halogen sources (Salawitch et al., 2005).

Figure 9.14 of IPCC (2007) suggests the stratospheric perturbation following the eruption of Pinatubo may not be handled particularly well by GCMs that contributed to IPCC (2007). This figure shows a dramatic drop in the height of the tropopause associated with enhanced SOD within GCMs that appears to be distinctly different than the observed, monthly mean tropopause height anomaly based on ECMWF 40 yr reanalysis (ERA-40). The modeled tropopause height anomaly shows GCMs tend to "collapse the tropopause" when SOD is enhanced. There is a sense of similar behavior in the observed tropopause after the eruption of Agung (although the observed perturbation is broader in time than the modeled response), opposite to observed behavior after El Chichón (i.e. observed tropopause rose at the time GCMs suggest it should have fallen), and a confused situation after Pinatubo. In early 1992, the reanalysis shows a well timed but smaller drop in the height of the tropopause than modeled; however, there are tropopause height transients before and after the eruption of Pinatubo in the reanalysis that are not apparent in the models. Perhaps these comparisons are affected by the low-pass filter applied to the data and model; the purpose of Fig. 9.14 is to document the importance of rising GHGs for the proper simulation of the long-term rise in tropopause height. Nonetheless, given the importance of proper quantification of the stratospheric response, future comparisons of modeled and measured tropopause height would be useful for evaluating and perhaps improving GCM simulations of the response of surface temperature to volcanic perturbations.

ACPD
12, 23829–23911, 2012

5.2 Implications for geo-engineering

The possibility of geo-engineering of climate via injection of sulfur to the stratosphere has a long history, starting with Budyko (1974), followed by a remarkably detailed and prescient chapter entitled "Geoengineering" in a National Academy of Sciences report (NAS, 1992), as well as papers by Dickinson (1996) and Schneider (1996). The suggestion by Crutzen (2006) that "if sizeable reductions in greenhouse gas emissions will not happen and temperatures rise rapidly, then climatic engineering" by artificial enhancement of stratospheric sulfate could be "the only option available to rapidly reduce temperature rises and counteract other climatic effects" led to a widespread renewal of interest in geo-engineering, undoubtedly due to the prominence of Paul Crutzen but also because cooling after the eruption of Pinatubo had been so well studied by the time his paper was written. Indeed, Crutzen (2006) wrote "enhanced reflection of solar radiation to space by the particles cooled the earth's surface on average by 0.5 °C in the year following the eruption" (of Pinatubo). Since 2006, many studies (e.g. Rasch et al., 2008a,b; Ammann et al., 2010) have estimated cooling due to stratospheric sulfate injection from first principles (i.e. optical properties of aerosols), rather than using $\Delta T_{\mathrm{VOLCANO}}$ inferred from Pinatubo. Nonetheless, Pinatubo as an analogy for geo-engineering of climate is pervasive in the modern literature: for instance, Robock et al. (2008) suggest the equivalent of one Pinatubo every 4–8 yr would be required to stop global warming (see also Robock et al., 2009).

If further studies support our suggestion that the cooling due to the eruption of Pinatubo has been over estimated by about a factor of 2, there are three important implications for geo-engineering of climate via injection of stratospheric sulfate. First, numerical values from past major volcanoes used as a proxy for cooling by geo-engineering would need to be revised. This revision would be straightforward to implement if consensus is achieved.

Second, the behavior of GCMs used to assess the response of climate to major volcanoes and the response of climate to geo-engineering will have to be critically

ACPD
12, 23829–23911, 2012

appraised. As described in Sect. 5.1, GCMs tend to strongly and consistently collapse the tropopause after major volcanic eruptions, a response not borne out by observation. The atmospheric sciences community has placed enormous effort towards evaluating the chemical, dynamical, and radiative behavior of chemistry-climate general circulation models (CCMs) (Eyring et al., 2010). However, none of the primary GCMs that have quantified volcanic cooling participated in the Eyring et al. (2010) effort. Chapter 4 of Eyring et al. (2010), entitled Stratospheric Dynamics, includes evaluative metrics for 13 CCMs, but does not include the GFDL GCM used by Soden et al. (2002) and Stenchikov et al. (2009), the NCAR PCM model of Wigley et al. (2005a), the HadCM3 model used by Forster and Collins (2004), or the HadGEM2-ES model of Booth et al. (2012). Given the importance of stratospheric dynamics for the quantification of both volcanic cooling and geo-engineering, we suggest the upcoming Geoengineering Model Intercomparison Project (GeoMIP) (Kravitz et al., 2011) adopt some of the evaluative metrics developed by Eyring et al. (2010) and apply these metrics to all GeoMIP GCMs. Representation of the response of stratospheric ozone to increased sulfate loading (Tilmes et al., 2008, 2009; Heckendorn et al., 2009) is also needed to properly forecast the response of surface temperature to geo-engineering, because ozone is the primary absorber of SW radiation in the stratosphere. Model representation of natural, very short lived (VSL) organic halogen sources may be necessary to properly treat the response of ozone to geo-engineering of climate, because ozone loss due to decomposition products of VSL halogen sources is acutely sensitive to aerosol loading in the lowermost stratosphere (Tilmes et al., 2012).

The third implication is subtle. Trenberth and Dai (2007) examined a 55 yr record of global land precipitation, river discharge, and the Palmer Drought Severity Index and concluded the eruption of Pinatubo led to precipitation and discharge anomalies much larger than those observed for other years, resulting in widespread drought. However, the AMO has also been associated with 20th century drought (e.g. Nigam et al., 2011). Figure 8 indicates the AMO was in a negative phase at the time Pinatubo erupted and that the transition from positive to negative started 2 yr prior to the eruption. If a

ACPD
12, 23829–23911, 2012

consensus emerges that the cold SSTs in the North Atlantic during 1992 were not caused entirely by Pinatubo, but instead were driven in part by a process such as sea ice export through the Fram Strait (Dima and Lohmann, 2007) or internal variability of salinity (Delworth and Zeng, 2012), then future analyses of the effects of Pinatubo on the hydrological cycle may have to isolate volcano and ocean induced perturbations to serve as a realistic proxy for geo-engineering.

6 Conclusions

The climate-record from 1900 to present exhibits a monotonic rise driven by increasing levels of anthropogenic GHGs (IPCC, 2007), sharp declines after major volcanic eruptions (Hansen et al., 1993; Lacis and Mischenchko, 1995; Soden et al., 2002), as well as an oscillation with a periodicity of 60 to 70 yr that has been attributed to variations in the strength of the Atlantic Meridional Overturning Circulation (AMOC) (Schlesinger and Ramankutty, 1994; Andronova and Schlesinger, 2000; Knight et al., 2005; Stouffer et al., 2006; Medhaug and Furevik, 2011). Prior studies that quantified volcanic cooling have not considered the effect of AMOC on global climate. We have shown, using multiple linear regression (MLR) analysis of many climate records, that cooling attributed to volcanic eruptions is reduced by about a factor of 2 when sea surface temperatures in the North Atlantic (the Atlantic Multidecadal Oscillation, or AMO) are used as a proxy for the effect of AMOC on global climate.

The surface temperature records from CRU4, GISS, NCDC, and BEG as well as lower tropospheric temperature from MSU, analyzed with the MLR model and excluding the AMO, yield values for the cooling associated with the eruption of Mount Pinatubo that range from 0.33 °C to 0.56 °C. This range is broadly consistent with values for Pinatubo cooling reported by Hansen et al. (1993), Lacis and Mischenchko (1995), and Soden et al. (2002). The cooling associated with Mount Pinatubo drops nearly a factor of 2, ranging from 0.15 °C to 0.36 °C, when these same data sets are analyzed

ACPD
12, 23829–23911, 2012

allowing for the influence of the AMOC in the regression (using AMO detrended by anthropogenic RF).

All of our modeled temperature anomalies drop by ~0.5 °C at the time of peak SOD following the eruption of Mount Pinatubo. However, we attribute a significant portion of this cooling to ocean circulation and not volcanoes, based on results of the regression analysis. The timing of stratospheric optical depth (SOD) and North Atlantic SST anomalies suggest changes in ocean circulation preceded the four major volcanic eruptions that have occurred since 1900. Hence, the data record suggests ocean circulation has affected prior estimates of volcanic cooling, rather than volcanic eruptions drive ocean circulation.

We use a detrended AMO as a proxy for the AMOC: i.e., this study focuses on variability of the AMOC, rather than possible long-term monotonic change in the strength of the AMOC. Nonetheless, precise determination of volcanic cooling is sensitive to the manner in which the AMO index is detrended. If global SST is used to detrend the AMO, as suggested by Trenberth and Shea (2006), the influence of the AMOC on volcanic cooling is moderate. On the other hand, if the AMO is detrended using either a linear regression (Enfield et al., 2001) or, as we suggest, anthropogenic radiative forcing of climate (which varies in a non-linear manner over time), then the influence of the AMOC on volcanic cooling is strong. The regression based on AMO detrended using anthropogenic RF simulates pre-WWI cooling and WWII warming of the CRU4 land temperature anomaly particularly well (Fig. 7d), giving credence to the possibility that variations in the strength of the AMOC have truly exerted influence on global climate and also that the AMO detrended using anthropogenic RF is a valid proxy for the AMOC. If a consensus emerges that variations in the strength of the Atlantic Meridional Overturning Circulation really do exert a major influence on global climate, as suggested by the regression analysis throughout this paper, then perhaps this provides an important new opportunity to improve estimates of temperature and climate on decadal time scales, as suggested by Knight et al. (2005).

ACPD
12, 23829–23911, 2012

If the factor of 2 reduction of volcanic cooling due to consideration of ocean circulation suggested here is borne out by future studies, the implications for geo-engineering of climate by artificial enhancement of stratospheric sulfate are immense. It would be straightforward to "recalibrate" Pinatubo as a proxy for geo-engineering. Of greater concern is the fidelity of atmospheric general circulation models (GCMs) used to assess the response of the atmosphere to major volcanoes as well as geo-engineering. Accurate GCM representation of the response to either perturbation requires realistic treatment of a myriad of physical processes, including the trapping of longwave thermal radiation by stratospheric sulfate aerosols, the dynamical response of the stratosphere, and changes in stratospheric ozone. The tendency of the GCMs used by IPCC (2007) to collapse the tropopause following major perturbations to SOD, which is not borne out by the ERA-40 reanalysis, suggests the physical response to stratospheric sulfate aerosol injection may not be properly represented in modern climate models.

Appendix A

Glossary of symbols

- α_{COOL}: parameter that scales the emission of all aerosol precursors that cool the atmosphere (negative RF) to total RF; units: $\mathrm{W\,m^{-2}\,Tg^{-1}}$
- α_{HEAT}: parameter that scales the emission of all aerosol precursors that cool the atmosphere (negative RF) to total RF; units: $\mathrm{W\,m^{-2}\,Tg^{-1}}$
- ΔT: Global, monthly mean temperature anomaly for either the surface or lower troposphere. Here, we consider four records of ΔT: the global surface (land and oceans), the land surface, the global lower troposphere (land and oceans), and the lower troposphere over land.

ACPD
12, 23829–23911, 2012

- $\Delta T_{2\times CO_2}$: Equilibrium climate sensitivity for a doubling of CO_2 relative to pre-industrial levels, which in our modeling framework is equal to $\lambda(1+\gamma)\Delta RF_{CO_2}$, where $\Delta RF_{CO_2} = 5.35\,W\,m^{-2}\,\ln(2)$ or $3.71\,W\,m^{-2}$; units: °C
- γ: sensitivity parameter representing the net effect of all feedbacks that occur in response to a GHG perturbation to RF; units: dimensionless
- λ: Response of surface temperature to a RF perturbation in the absence of any feedbacks, for Earth's present-day overall albedo; value set at $0.3\,°C/W\,m^{-2}$ throughout
- $\lambda(1+\gamma)$: climate sensitivity in response to a GHG perturbation to RF; units: $°C/W\,m^2$
- AF: Anthropogenic radiative forcing of climate
- AMO: Atlantic Multidecadal Oscillation
- $AMO_{Had3\ AF}$: AMO found by detrending monthly mean SST in the Atlantic, from 0 to 60° N, based on the HadSST3 record using anthropogenic forcing of climate (GHG RF + NAA RF); units: °C
- $AMO_{Had3\ LIN}$: AMO found by detrending monthly mean SST in the Atlantic, from 0 to 60° N, based on the HadSST3 record, using a linear regression; units: °C
- $AMO_{Had3\ SST}$: AMO found by detrending monthly mean SST in the Atlantic, from 0 to 60° N, based on the HadSST3 record, using global SST (also from HadSST3); units: °C
- AMOC: Atlantic Meridional Overturning Circulation
- CRU: Climate Research Unit, University of East Anglia
- GCM: Atmosphere ocean general circulation model

ACPD
12, 23829–23911, 2012

- ECMWF: European Centre for Medium-Range Weather Forecasts
- ENSO: El Niño-Southern Oscillation or El Niño-Southern Oscillation Index, units: dimensionless
- ERA-40: ECMWF 40 yr Re-Analysis
- GCM: General Circulation Model
- GHG RF: Direct RF due to Greenhouse Gases, here taken to be CO_2, CH_4, Tropospheric O_3, Halocarbons, and N_2O
- HadSST3: Latest sea surface temperature record from the Hadley Centre
- KaplanSST2: Latest sea surface temperature record from NOAA, which they call Kaplan Extended SST V2
- LW: Longwave or thermal radiation
- MLR: Multiple Linear Regression
- MSU: Microwave Sounding Unit
- NAA RF: Net Anthropogenic Aerosol RF; units: $W m^{-2}$
- OHC: Ocean Heat Content of the upper 700 m of the global ocean; units: J
- OHE: Ocean Heat Export (the derivative of OHC); units: $W m^{-2}$
- Q_{OCEAN}: Model representation of Ocean Heat Export; units: $W m^{-2}$
- RCP: Representative Concentration Pathways
- RF: stratospheric-adjusted radiative forcing of climate, as described in Sect. 2.2 of IPCC, 2007; units: $W m^{-2}$

ACPD
12, 23829–23911, 2012

- $RF_{SULATE-DIR}$: Direct RF due to sulfate aerosols; units: $W m^{-2}$
- $RF_{SULATE-TOT}$: Total RF due to sulfate aerosols; units: $W m^{-2}$
- S_{EMISS}: Emission of sulfur, a precursor of sulfate aersols; units: $Tg yr^{-1}$
- SOD: Stratospheric Optical Depth; units: dimensionless
- SST: Sea Surface Temperature; units: °C
- SW: Short wave or solar radiation
- TSI: Total Solar Irradiance: units: $W m^{-2}$

Appendix B

Websites

ΔT, surface

- CRU4
  HadCRUT4 (global): http://www.metoffice.gov.uk/hadobs/hadcrut4
  CRUTEM4 (land): http://www.cru.uea.ac.uk/cru/data/temperature
- GISS: http://data.giss.nasa.gov/gistemp
- NCDC: http://www.ncdc.noaa.gov/cmb-faq/anomalies.php
- BEG: http://berkeleyearth.org/

ΔT, atmosphere

- MSU (global): http://vortex.nsstc.uah.edu/data/msu/t2lt/tltglhmam_5.4

ACPD
12, 23829–23911, 2012

- MSU (land): http://www.remss.com/data/msu/monthly_time_series/RSS_Monthly_MSU_AMSU_Channel_TLT_Anomalies_Land_v03_3.txt

Ocean Heat Content

- Church: http://www.cmar.csiro.au/sealevel/TSL_OHC_20110926.html
- Gouretski and Reseghetti (2010): http://www1.ncdc.noaa.gov/pub/data/cmb/bams-sotc/2009/global-data-sets/OHC_viktor.txt

Ocean Indices

- ENSO: http://www.esrl.noaa.gov/psd/enso/mei
- PDO: http://jisao.washington.edu/pdo/
- IOD: http://www.jamstec.go.jp/frsgc/research/d1/iod/e/iod/dipole_mode_index.html

Radiation Budget

- ERBE: http://eosweb.larc.nasa.gov/PRODOCS/erbe/edition3_rev1/access_ed3_rev1_data.html

RCP

- Mixing ratios of CO_2, CH_4, N_2O, and certain halocarbons are from: http://www.iiasa.ac.at/web-apps/tnt/RcpDb

RCP Potsdam

- RF due to tropospheric O_3 and direct RF due to aerosol components, other than sulfate for the past, are from: http://www.pik-potsdam.de/~mmalte/rcps
- $RF_{SULATE-TOT}$ http://www.sterndavidi.com/Data/Climate.xls

SOD

- GISS: http://data.giss.nasa.gov/modelforce/strataer

ACPD
12, 23829–23911, 2012

– NOAA: ftp://ftp.ncdc.noaa.gov/pub/data/paleo/climate_forcing/volcanic_aerosols/ammann2003b_volcanics.txt

TSI:

– Up to end of 2008: ftp://strat50.met.fu-berlin.de/pub/outgoing/_matthes/CMIP5_solardata/TSI_WLS_mon_1882_2008.txt

– After 2008: ftp://ftp.pmodwrc.ch/pub/data/irradiance/composite

Note: in the submitted version of the paper, we use a record for TSI sent to us by J. Lean, personal communication, 2012 that covers the 1900 to 2011 period. There is no significant difference between the TSI record from Lean and the concatenation of the two records given above.

Appendix C

Uncertainty of regression coefficients

The Interactive Data Language (IDL®) program regress.pro also returns uncertainties for the regression coefficients, $C_{j,\ j=0\ \text{to}\ 6}$, based on well established statistical methods. The approach is described in Sect. 9.2 of Draper and Smith (1998). Briefly, the uncertainties for regression coefficient C_j, denoted σ_{Cj}, is found from:

$$\sigma_{Cj} = (\mathbf{V}_{j,\ j})^{0.5} \tag{C1}$$

where $\mathbf{V}$ is the variance-covariance matrix of the regression coefficients:

$$\mathbf{V} = (R^T \mathbf{W}^{-1} R)^{-1} (\sigma_{MEAN})^2 \tag{C2}$$

where:

ACPD
12, 23829–23911, 2012

In this notation:

$$\sigma_{\mathrm{MEAN}} = \frac{1}{N_{\mathrm{MONTHS}}} \sum_{i=1}^{N_{\mathrm{MONTHS}}} \sigma_{\mathrm{OBS}\ i} \tag{C3}$$

R is the matrix of regressor variables (rows are time, columns are SOD, TSI, ENSO, etc), and

W is the diagonal matrix of weights given by:

$$\mathbf{W} = \begin{bmatrix} \frac{1}{w_1} & \cdots & 0 \\ \vdots & \ddots & \vdots \\ 0 & \cdots & \frac{1}{w_{N_{\mathrm{MONTHS}}}} \end{bmatrix} \tag{C4}$$

where:

$$w_i = \frac{\sigma^2_{\mathrm{OBS}\ i}}{\sigma_{\mathrm{MEAN}}} \tag{C5}$$

We programmed Eqs. (A1) to (A5) and computed values of $\sigma_{\mathrm{C}j}$ to confirm the behavior of IDL® program regress.pro.

Appendix D

NAA RF_{2005} range and uncertainty

The magnitude of net anthropogenic aerosol radiative forcing (NAA RF) is important for understanding climate change, yet as described in Sect. 2.4 of IPCC (2007), the value of NAA RF is highly uncertain. We have developed a parameterization, based on scaling coefficients α_{COOL} and α_{HEAT}, to span the uncertainty of NAA RF in our model.

ACPD
12, 23829–23911, 2012

As explained in the paper, the value of NAA RF in year 2005, denoted NAA RF_{2005}, is used as a benchmark for NAA RF as a function of time due to the large number of tables and figures in IPCC (2007) that quantify RF of anthropogenic aerosols between 1750 and 2005.

Here, we describe how we have used Table 2.12 of IPCC (2007) to arrive at a "best estimate" for NAA RF_{2005} of $-1.0\,W\,m^{-2}$, with a range of $-2.2\,W\,m^{-2}$ to $-0.4\,W\,m^{-2}$. Table 2.12 gives best estimates of global mean radiative forcing, from 1750 to 2005, for direct RF from sulfate, fossil fuel OC, fossil fuel BC, biomass, nitrate, and mineral dust aerosols as well as cloud albedo affect, surface albedo change due to BC on snow, and contrails. Summing the 9 values for these best estimates given in the AR4 column yields a change in global mean RF, from 1750 to 2005, of $-1.03\,W\,m^{-2}$. We round this to $-1.0\,W\,m^{-2}$. Assuming the effect of anthropogenic aerosols on climate in year 1750 was zero, we arrive at a best estimate of $-1.0\,W\,m^{-2}$ for NAA RF_{2005}.

Table 2.12 of IPCC (2007) also gives 2σ estimated uncertainties for each component in Table 2.12. For some of the components the uncertainties are not symmetric about the best estimate. The square root of the sum of squares of the upper limits (most cooling) of the uncertainties for aerosol cooling, for the 9 terms noted above, yields $1.16\,W\,m^{-2}$. The square root of the sum of squares of the lower limits (least cooling) of the uncertainties for aerosol cooling yields $0.55\,W\,m^{-2}$. We round these numbers to $1.2\,W\,m^{-2}$ and $0.6\,W\,m^{-2}$.

Combining these numbers the best estimate for NAA RF_{2005} is $-1.0\,W\,m^{-2}$, with a range of uncertainty extending from $-2.2\,W\,m^{-2}$ ($-1.0-1.2=-2.2$) to $-0.4\,W\,m^{-2}$ ($-1.0+0.6=-0.4$). This range of uncertainty is denoted "Empirical Range" on Fig. 4 and in the text, since it is based on analyses of aerosol, cloud, and surface data.

Supplementary material related to this article is available online at: http://www.atmos-chem-phys-discuss.net/12/23829/2012/acpd-12-23829-2012-supplement.pdf.

ACPD
12, 23829–23911, 2012

Acknowledgements. We appreciate constructive criticism provided by Daniel Kirk-Davidoff that motivated examination of the sensitivity of the volcanic regression coefficient to the manner upon which the AMO was detrended. We appreciate helpful email exchanges with John Daniel, Jean-Francois Lamarque, Judith Lean, Malte Meinshausen, Steven Montzka, Alan Robock, Georgiy Stenchikov, David Stern, Guus Velders, and Thomas Wigley at various stages of this study. Comments from colleagues at the 2011 Santa Fe Conference on Global and Regional Climate Change are also appreciated.

References

Ammann, C. M., Meehl, G. A., Washington, W. M., and Zender, C. S.: A monthly and latitudinally varying volcanic forcing dataset in simulations of 20th century climate, Geophys. Res. Lett., 30(12), 1657, doi:10.1029/2003GL016875, 2003.

Ammann, C. M., Washington, W. M., Meehl, G. A., Buja, L., and Teng, H: Climate engineering through artificial enhancement of natural forcings: magnitudes and implied consequences, J. Geophys. Res., 115, D22109, doi:10.1029/2009JD012878, 2010.

Andronova, N. G. and Schlesinger, M. E.: Causes of global temperature changes during the 19th and 20th centuries, Geophys. Res. Lett., 27(14), 2137–2140, doi:10.1029/2000GL006109, 2000.

Bony, S., Colman, R., Kattsov, V. M., Allan, R. P., Bretherton, C. S., Dufresne, J.-L., Hall, A., Hallegatte, S., Holland, M. M., Ingram, W., Randall, D. A., Soden, B. J., Tselioudis, G., Webb, M. J.: How well do we understand and evaluate climate change feedback processes?, J. Clim., 19, 3445–3482, doi:10.1029/2005GL023851, 2006.

Booth, B. B. B., Dunstone, N. J., Halloran, P. R., Andrews, T., and Bellouin, N.: Aersosols implicated as a prime driver of twentieth-century North Atlantic climate variability, Nature, 484, 228–232, doi:10.1038/nature10946, 2012.

Budyko, M. I.: Climate and Life, Academic, New York, 508 pp., 1974.

Carton, J. A. and Santorelli, A.: Global upper ocean heat content as viewed in nine analyses, J. Clim., 21, 6015–6035. doi:10.1175/2008JCLI2489.1, 2008.

Chavez, F. P., Ryan, J., Lluch-Cota, S. E., Ñiquen C. M.: From anchovies to sardines and back: multidecadal change in the Pacific Ocean, Science, 299, 217–221, doi:10.1126/science.1075880, 2003.

ACPD

12, 23829–23911, 2012

Christy, J. R., Spencer, R. W., and Braswell, W. D.: MSU tropospheric temperatures: dataset construction and radiosonde comparisons, J. Atmos. Ocean. Technol., 17, 1153–1170, 2000.
Christy, J. R., Spencer, R. W., Norris, W. B., Braswell, W. D., and Parker, D. E.: Error estimates of Version 5.0 of MSU–AMSU bulk atmospheric temperatures, J. Atmos. Oceanic Technol., 20, 613–629, 2003.
Church, J. A., White, N. J., and Arblaster, J. M.: Significant decadal–scale impact of volcanic eruptions on sea level and ocean heat content, Nature, 438, 74–77, doi:10.1038/nature04237, 2005.
Church, J. A., White, N. J., Konikow, L. F., Domingues, C. M., Cogley, J. G., Rignot, E., Gregory, J. M., van den Broecke, M. R., Monaghan, A. J., and Velicogna, I.: Revisiting the Earth's sea-level and energy budgets from 1961 to 2008, Geophys. Res. Lett., 38, L18601, doi:10.1029/2011GL048794, 2011.
Crutzen, P. J.: Albedo enhancement by stratospheric sulfur injections: a contribution to resolve a policy dilemma?, Clim. Change, 77, 211–220, doi:10.1007/s10584-006-9101-y, 2006.
Davies, R. and Molloy, M.: Global cloud height fluctuations measured by MISR on Terra from 2000 to 2010, Geophys. Res. Lett., 39, L03701, doi:10.1029/2011GL050506, 2012.
DeLand, M. T. and Cebula, R. P.: Solar UV variations during the decline of cycle 23, J. Atmos. Sol. Terr. Phys., 77, 225–234, doi:10.1016/j.jastp.2012.01.007, 2012.
Delworth, T. L. and Zeng, F.: Multicentennial variability of the Atlantic meridional overturning circulation and its climatic influence in a 4000 yr simulation of the GFDL CM2.1 climate model, Geophys. Res. Lett., 39, L13702, doi:10.1029/2012GL052107, 2012.
Dickinson, R. E.: Climate engineering: a review of aerosol approaches to changing the global energy balance, Clim. Change, 33, 279–290, doi:10.1007/BF00142576, 1996.
Dima, M. and Lohmann, G.: A Hemispheric mechanism for the Atlantic Multidecadal Oscillation, J. Clim., 20, 2706–2719, doi:10.1175/JCLI4174.1, 2007.
Domingues, C. M., Church, J. A., White, N. J., Glecker, P. J., Wijffels, S. E., Barker, P. M., and Dunn, J. R.: Improved estimates of upper-ocean warming and multidecadal sea-level rise, Nature, 453, 1090–1093, doi:10.1038/nature07080, 2008.
Douglass, D. H. and Knox, R. S.: Climate forcing by the volcanic eruption of Mount Pinatubo, Geophys. Res. Lett., 32, L05710, doi:10.1029/2004GL022119, 2005.
Draper, N. R. and Smith, H.: Applied Regression Analysis, 3rd edn., J. Wiley and Sons, New York, 1998.

ACPD
12, 23829–23911, 2012

Dutton, E. G. and Bodhaine, B. A.: Solar irradiance anomalies caused by clear-sky transmission variations above Mauna Loa: 1958–1999, J. Clim., 14, 3255–3262, 2001.
Enfield, D. B., Mestas-Nuñez, A. M., and Trimble, P. J.: The Atlantic Multidecadal Oscillation and its relation to rainfall and river flows in the continental U. S., Geophys. Res. Lett. 28, 2077–2080, doi:10.1029/2000GL012745, 2001.
Eyring, V., Shepherd, T. G., and Waugh, D. W. (eds.): SPARC Report on the Evaluation of Chemistry-Climate Models, SPARC Report No. 5, WCRP-132, WMO/TD-No. 1526, 2010.
Forster, P. M. de F. and Collins, M.: Quantifying the water vapour feedback associated with post-Pinatubo global cooling, Clim. Dyn., 23, 207–214, doi:10.1007/s00382-004-0431-z, 2004.
Forster, P. M. de F. and Gregory, J. M.: The climate sensitivity and its components diagnosed from Earth radiation budget data, J. Clim., 19, 39–52, doi:10.1175/JCLI3611.1, 2006.
Gouretski, V. and Reseghetti, F.: On depth and temperature biases in bathythermograph data: development of a new correction scheme based on analysis of a global ocean database, Deep-Sea Res. I, 57, 812–833, doi:10.1016/j.dsr.2010.03.011, 2010.
Guan, B. and Nigam, S.: Analysis of Atlantic SST variability factoring interbasin links and the secular trend: clarified structure of the Atlantic Multidecadal Oscillation, J. Clim., 22, 4228–4240, doi:10.1175/2009JCLI2921.1, 2009.
Hansen, J. E., Lacis, A., Rind, D., Russell, G., Stone, P., Fung, I., Ruedy, K., and Lerner, J.: Climate sensitivity: analysis of feedback mechanisms, Amer. Geophys. Union, Monogr. Ser., 29, 130–163, 1984.
Hansen, J., Lacis A., Ruedy, R., Sato, M., and Wilson H.: How sensitive is the world's climate?, Natl. Geog. Soc. Res. Exploration, 9, 142–158, 1993.
Hansen, J., Sato, M., Ruedy, R., Lo, K., Lea, D. W., and Medina-Elizade, M.: Global temperature change, Proc. Nat. Acad. Sci., 103(39), 14288–14293, doi:10.1073/pnas.0606291103, 2006.
Hansen, J., Ruedy, R., Sato, M., and Lo, K.: Global surface temperature change, Rev. Geophys., 48, RG4004, doi:10.1029/2010RG000345, 2010.
Harries, J. E. and Futyan, J. M.: On the stability of the Earth's radiative energy balance: response to the Mt. Pinatubo eruption, Geophys. Res. Lett. 33, L23814, doi:10.1029/2006GL027457, 2006.
Heckendorn P., Weisenstein, D., Fueglistaler, S., Luo, B. P., Rozanov, E., Shraner, M., Thomason, L. W., and Peter, T.: The impact of geoengineering aerosols on stratospheric temperature and ozone, Environ. Res. Lett., 4, 045108, doi:10.1088/1748-9326/4/4/045108, 2009.

ACPD
12, 23829–23911, 2012

IPCC, 2001: Climate Change 2001: The Scientific Basis. Contribution of Working Group I to the Third Assessment Report of the Intergovernmental Panel on Climate Change, edited by: Houghton, J. T., Ding, Y., Griggs, D. J., Noguer, M., van der Linden, P. J., Dai, X., Maskell, K., and Johnson, C. A., Cambridge University Press, Cambridge, UK and New York, NY, USA, 881 pp., 2001.

IPCC, 2007: Climate Change 2007: The Physical Science Basis. Contribution of Working Group I to the Fourth Assessment Report of the Intergovernmental Panel on Climate Change edited by: Solomon, S., Qin, D., Manning, M., Chen, Z., Marquis, M., Averyt, K. B., Tignor, M., and Miller, H. L., Cambridge University Press, Cambridge, UK and New York, NY, USA, 996 pp., 2007.

Iwi, A. M., Hermanson, L., Haines, K., and Sutton, R. T.: Mechanisms linking volcanic aerosols to the Atlantic meridional overturning circulation, J. Climate, 25, 3039–3051, 2012.

Jones, P. D., Lister, D. H., Osborn, T. J., Harpham C., Salmon, M., and Morice, C. P.: Hemispheric and large-scale land-surface air temperature variations: an extensive revision and an update to 2010, J. Geophys. Res., 117, D05127, doi:10.1029/2011JD017139, 2012.

Kennedy, J. J., Rayner, N. A., Smith, R. O., Saunby, M., and Parker, D. E.: Reassessing biases and other uncertainties in sea-surface temperature observations since 1850 part 1: measurement and sampling errors, J. Geophys. Res., 116, D14103, doi:10.1029/2010JD015218, 2011a.

Kennedy, J. J., Rayner, N. A., Smith, R . O., Saunby, M., and Parker, D. E.: Reassessing biases and other uncertainties in sea-surface temperature observations since 1850 part 2: biases and homogenization, J. Geophys. Res., 116, D14104, doi:10.1029/2010JD015220, 2011b.

Kiehl, J. T.: Twentieth century climate model response and climate sensitivity, Geophys. Res. Lett., 34, L22710, doi:10.1029/2007GL031383, 2007.

Kinne, S., Toon, O. B., and Prather, M.: Buffering of stratospheric circulation by changing amounts of tropical ozone: a Pinatubo case study, Geophys. Res. Lett., 19, 1927–1930, doi:10.1029/92GL01937, 1992.

Kinnison, D. E., Grant, K. E., Connell, P. S., Wuebbles, D. J., and Rotman, D. A.: The chemical radiative effects of the Mt. Pinatubo eruption, J. Geophys. Res., 99, 25705–25731, doi:10.1029/94JD02318, 1994.

Knight J. R., Allan, R. J., Folland, C. K., Vellinga, M., and Mann, M. E.: A signature of persistent natural thermohaline circulation cycles in observed climate, Geophys. Res. Lett., 32, L20708, doi:10.1029/2005GL024233, 2005.

ACPD
12, 23829–23911, 2012

Knutti, R. and Hegerl, G. C.: The equilibrium sensitivity of the Earth's temperature to radiation changes, Nature Geosci., 1, 735–743, doi:10.1038/ngeo337, 2008.
Kopp, G. and Lean, J. L.: A new, lower value of total solar irradiance: evidence and climate significance, Geophys. Res. Lett., 38, L01706, doi:10.1029/2010GL045777, 2011.
Kravitz, B., Robock, A., Boucher, O., Schmidt, H., Taylor, K. E., Stenchikov, G., and Schulz, M.: The geo-engineering model intercomparison project (GeoMIP), Atmos. Sci. Lett., 12, 162–167, doi:10.1002/asl.316, 2011.
Kuhlbrodt, T., Griesel, A., Montoya, M., Levermann, A., Hofmann, M., and Rahmstorf, S.: On the driving processes of the Atlantic meridional overturning circulation, Rev. Geophys., 45, RG2001, doi:10.1029/2004RG000166, 2007.
Lacis, A. A. and Mishchenko, M. I.: Climate forcing, climate sensitivity, and climate response: a radiative modeling perspective on atmospheric aerosols, in: Aerosol Forcing of Climate: Report of the Dahlem Workshop on Aerosol Forcing of Climate, edited by: Charlson, R. J., and Heintzenberg, J., 11–42, John Wiley Sons, Chichester, England/New York, 1995.
Lamarque, J.-F., Kyle, G., Meinshausen, M., Riahi, K., Smith, S., van Vuuren, D., Conley, A., and Vitt, F.: Global and regional evolution of short-lived radiatively-active gases and aerosols in the representative concentration pathways, Climatic Change, 109, 191–212, doi:10.1007/s10584-011-0155-0, 2011.
Lean, J. L.: Evolution of the Sun's spectral irradiance since the Maunder minimum, Geophys. Res. Lett., 27(16), 2425–2428, doi:10.1029/2000GL000043, 2000.
Lean, J. L. and DeLand, M. T.: How does the Sun's spectrum vary?, J. Climate, 25, 2555–2560, doi:10.1175/JCLI-D-11-00571.1, 2012.
Lean, J. L. and Rind, D. H.: How natural and anthropogenic influences alter global and regional surface temperatures: 1889 to 2006, Geophys. Res. Lett., 35, L18701, doi:10.1029/2008GL034864, 2008.
Mascioli, N. R., Canty, T., and Salawitch, R. J., An empirical model of global climate – Part 2: Implications for future temperature, Atmos. Chem. Phys. Discuss., 12, 23913–23974, doi:10.5194/acpd-12-23913-2012, 2012.
Mass, C. F. and Portman, D. A.: Major volcanic eruptions and climate: a critical evaluation, J. Clim., 2, 566–593, 1989.
McGuffie, K. and Henderson-Sellers, A.: A Climate Modeling Primer, 3rd edn., J. Wiley and Sons, Chichester, England, 2005.

ACPD
12, 23829–23911, 2012

Medhaug, I. and Furevik, T.: North Atlantic 20th century multidecadal variability in coupled climate models: sea surface temperature and ocean overturning circulation, Ocean Sci., 7, 389–404, doi:10.5194/os-7-389-2011, 2011.
Meehl, G., Arblaster, J., Fasullo, J., Hu, A., and Trenberth, K.: Model-based evidence of deep-ocean heat uptake during surface-temperature hiatus periods, Nature Clim. Change, 1, 360–364. doi:10.1038/nclimate1229, 2011.
Meinshausen, M., Smith, S. J., Calvin, K. V., Daniel, J. S., Kainuma, M. L. T., Lamarque, J.-F., Matsumoto, K., Montzka, S., Raper, S., Riahi, K., Thomson, A. M., Velders, G. J. M., and van Vuuren, D. P.: The RCP greenhouse gas concentrations and their extensions from 1765 to 2300, Climatic Change, 109, 213–241, doi:10.1007/s10584-011-0156-z, 2011.
Morice, C. P., Kennedy, J. J., Rayner, N. A., and Jones, P. D., Quantifying uncertainties in global and regional temperature change using an ensemble of observational estimates: the HadCRUT4 data set, J. Geophys. Res., 117, D08101, doi:10.1029/2011JD017187, 2012.
Murphy, D. M., Solomon, S., Portmann, R. W., Rosenlof, K. H., Forster, P. M., and Wong, T.: An observationally based energy balance for the Earth since 1950, J. Geophys. Res., 114, D17107, doi:10.1029/2009JD012105, 2009.
Myhre, G., Highwood, E. J., Shine, K. P., and Stordal, F.: New estimates of radiative forcing due to well mixed greenhouse gases, Geophys. Res. Lett., 25, 2715–2718, doi:10.1029/98GL01908, 1998.
Myhre, G., Myhre, A., and Stordal, F.: Historical evolution of radiative forcing of climate, Atmos. Environ., 35, 2361–2373, doi:10.1016/S1352-2310(00)00531-8, 2001.
National Academy of Sciences (NAS): Policy Implications of Greenhouse Warming: Mitigation, Adaptation, and the Science Base, Panel on Policy Implications of Greenhouse Warming, National Academy Press, Washington, DC, 1992.
Nigam, S., Guan, B., and Ruiz-Barradas, A.: Key role of the Atlantic Multidecadal Oscillation in 20th century drought and wet periods over the Great Plains, Geophys. Res. Lett., 38, L16713, doi:10.1029/2011GL048650, 2011.
Rasch, P. J., Crutzen, P. J., and Coleman, D. B.: Exploring the geoengineering of climate using stratospheric sulfate aerosols: the role of particle size, Geophys. Res. Lett., 35, L02809, doi:10.1029/2007GL032179, 2008a.
Rasch, P. J., Tilmes, S., Turco, R. P., Robock, A., Oman, L., and Chen, C.-C.: An overview of geoengineering of climate using stratospheric sulphate aerosols, Philos. Trans. R. Soc., Ser. A., 366, 4007–4037, doi:10.1098/rsta.2008.0131, 2008b.

ACPD
12, 23829–23911, 2012

Riahi, K., Grüber, A., and Nakicenovic, N.: Scenarios of long-term socio-economic and environmental development under climate stabilization, Technol. Forecast. Soc. Change 74, 887–935, doi:10.1016/j.techfore.2006.05.026, 2007.

Riahi, K., Rao, S., Krey, V., Cho, C., Chirkov, V., Fischer, G., Kindermann, G., Nakicenovic, N., and Rafaj, P.: RCP 8.5 – a scenario of comparatively high greenhouse gas emissions, Climatic Change, 109, 33–57, doi:10.1007/s10584-011-0149-y, 2011.

Robock, A., Oman, L., and Stenchikov, G. L.: Regional climate responses to geoengineering with tropical and Arctic SO_2 injections, J. Geophys. Res., 113, D16101, doi:10.1029/2008JD010050, 2008.

Robock, A., Marquardt, A., Kravitz, B., and Stenchikov, G.: Benefits, risks, and costs of stratospheric geoengineering, Geophys. Res. Lett., 36, L19703, doi:10.1029/2009GL039209, 2009.

Rohde, R., Curry, J., Groom, D., Jacobsen, R., Muller, R. A., Perlmutter, S., Rosenfeld, A., Wickham, C., and Wurtele, J.: Berkeley Earth temperature averaging process, J. Geophys Res. available at: http://berkeleyearth.org/available-resources, (last access: 11 July 2012), in press, 2011.

Saji, H. H., Goswami, B. N., Vinayachandran, P. H., and Yamagata, T.: A dipole mode in the tropical Indian Ocean, Nature, 401, 360–363, doi:10.1038/43854, 1999.

Salawitch, R. J., Weisenstein, D. K., Kovalenko, L. J., Sioris, C. E., Wennberg, P. O., Chance, K., Ko, M. K. W., and McLinden, C. A.: Sensitivity of ozone to bromine in the lower stratosphere, Geophys. Res. Lett., 32, L05811, doi:10.1029/2004GL021504, 2005.

Saravanan, R., and McWilliams, J. C.: Advective ocean–atmosphere interaction: an analytical stochastic model with implications for decadal variability, J. Clim., 11, 165–188, 1998.

Sato, M., Hansen, J. E., McCormick, M. P., and Pollack, J. B.: Stratospheric aerosol optical depths, 1850–1990. J. Geophys. Res., 98, 22987–22994, doi:10.1029/93JD02553, 1993.

Schlesinger, M. E. and Ramankutty, N.: An oscillation in the global climate system of period 65–70 years, Nature, 367, 723–726, doi:10.1038/367723a0, 1994.

Schoeberl, M. R., Bhartia, P. K., Hilsenrath, E., and Torres, O.: Tropical ozone loss following the eruption of Mt. Pinatubo, Geophys. Res. Lett., 20, 29–32, doi:10.1029/92GL02637, 1993.

Schneider, S. H.: Geoengineering: could-or should-we do it?, Clim. Change, 33, 291–302, doi:10.1007/BF00142577, 1996.

ACPD

12, 23829–23911, 2012

Schwartz, S. E.: Determination of Earth's transient and equilibrium climate sensitivities from observations over the twentieth century: strong dependence on assumed forcing, Surv. Geophys., 33, 745–777, doi:10.1007/s10712-012-9180-4, 2012.
Shindell, D., Faluvegi, G., Lacis, A., Hansen, J., Ruedy, R., and Aguilar, E.: Role of tropospheric ozone increases in 20th-century climate change, J. Geophys. Res., 111, D08302, doi:10.1029/2005JD006348, 2006.
Smith, S. J., van Aardenne, J., Klimont, Z., Andres, R. J., Volke, A., and Delgado Arias, S.: Anthropogenic sulfur dioxide emissions: 1850–2005, Atmos. Chem. Phys., 11, 1101–1116, doi:10.5194/acp-11-1101-2011, 2011.
Smith, T. M. and Reynolds, R. W.: A global merged land-air-sea surface temperature reconstruction based on historical observations (1880–1997), J. Clim., 18, 2021–2035, doi:10.1175/JCLI3362.1, 2005.
Smith, T. M., Reynolds, R. W., Peterson, T. C., and Lawrimore, J.: Improvements to NOAA's historical merged land-ocean surface temperature analysis (1880–2006), J. Clim., 21, 2283–2296, doi:10.1175/2007JCLI2100.1, 2008.
Soden, B. J. and Held, I. M.: An assessment of climate feedbacks in coupled atmosphere–ocean models, J. Clim., 19, 3354–3360, doi:10.1175/JCLI3799.1, 2006.
Soden, B. J., Wetherald, R. T., Stenchikov, G. L., and Robock A.: Global cooling after the eruption of Mount Pinatubo: a test of climate feedback by water vapor, Science, 296, 727–730, doi:10.1126/science.296.5568.727, 2002.
Solomon, S., Daniel, J. S., Sanford, T. J., Daniel, M., Murphy, D. M., Plattner, G.-K., Knutti, R., and Friedlingstein, P.: Persistence of climate changes due to a range of greenhouse gases, Proc. Natl. Acad. Sci. USA, 107, 18354–18359, doi:/10.1073/pnas.1006282107, 2010.
Stenchikov, G., Delworth, T. L., Ramaswamy, V., Stouffer, R. J., Wittenberg, A., and Zeng, F.: Volcanic signals in oceans, J. Geophys. Res., 114, D16104, doi:10.1029/2008JD011673, 2009.
Stern, D. I.: An atmosphere-ocean time series model of global climate change, Comput. Stat. Data An., 51, 1330–1346, doi:10.1016/j.csda.2005.09.016, 2006a.
Stern, D. I.: Reversal of the trend in global anthropogenic sulfur emissions, Chemosphere, 16, 207–220, doi:10.1016/j.gloenvcha.2006.01.001, 2006b.
Stouffer, R. J., Yin, J., Gregory, J. M., Dixon, K. W., Spelman, M. J., Hurlin, W., Weaver, A. J., Eby, M., Flato, G. M., Hasumi, H., Hu, A., Jungclaus, J. H., Kamenkovich, I. V., Levermann, A., Montoya, M., Murakami, S., Nawrath, S., Oka, A., Peltier, W. R., Robitaille, D. Y.,

ACPD
12, 23829–23911, 2012

Sokolov, A., Vettoretti, G., and Webber, S. L.: Investigating the causes of the response of the thermohaline circulation to past and future climate changes, J. Clim., 19, 1365–1387, doi:10.1175/JCLI3689.1, 2006.

Thompson, D. W. J., Kennedy, J. J., Wallace, J. M., and Jones, P. D.: A large discontinuity in the mid-twentieth century in observed global-mean surface temperature, Nature, 453, 646–649, doi:10.1038/nature06982, 2008.

Thompson, R. D.: Volcanic eruptions and global temperatures, Ambio, 24, 320–321, 1995.

Tilmes, S., Müller, R., and Salawitch, R.: The sensitivity of polar ozone depletion to proposed geoengineering schemes, Science, 320, 1201–1204, doi:10.1126/science.1153966, 2008.

Tilmes, S., Garcia, R. R., Kinnison, D. E., Gettelman, A., and Rasch, R. J.: Impact of geo-engineered aerosols on the troposphere and stratosphere, J. Geophys. Res., 114, D12305, doi:10.1029/2008JD011420, 2009.

Tilmes, S., Kinnison, D. A., Garcia, R., Salawitch, R., Canty, T., Lee-Taylor, J., Madronich, S., and Chance, K.: Impact of very short-lived halogens on stratospheric ozone abundance and UV radiation in a geo-engineered atmosphere, Atmos Chem. Phys. Discuss., 12, 21923–21945, doi:10.5194/acpd-12-21923-2012, 2012.

Ting, M., Kushnir, Y., Seager, R., and Li, C.: Forced and internal twentieth-century SST trends in the North Atlantic, J. Clim., 22, 1469–1481, doi:10.1175/2008JCLI2561.1, 2009.

Trenberth, K. E. and Dai, A.: Effects of Mount Pinatubo volcanic eruption on the hydrological cycle as an analog of geoengineering, Geophys. Res. Lett. 34, L15702, doi:10.1029/2007GL030524, 2007.

Trenberth, K. E. and Shea, D. J.: Atlantic hurricanes and natural variability in 2005, Geophys. Res. Lett., 33, L12704, doi:10.1029/2006GL026894, 2006.

van Oldenborgh, G. J., te Raa, L. A., Dijkstra, H. A., and Philip, S. Y.: Frequency- or amplitude-dependent effects of the Atlantic meridional overturning on the tropical Pacific Ocean, Ocean Sci., 5, 293–301, doi:10.5194/os-5-293-2009, 2009.

van Vuuren, D. P., Edmonds, J. A., Kainuma, M., Riahi, K., Thomson, A. M., Hibbard, K., Hurtt, G. C., Kram, T., Krey, V., Lamarque, J.-F., Masui, T., Meinshausen, M., Nakicenovic, N., Smith, S. J., and Rose, S: The representative concentration pathways: an overview, Climatic Change, 109, 5–31, doi:10.1007/s10584-011-0148-z, 2011.

Velders, G. J. M., Fahey, D. W., Daniel, J. S., McFarland, M., and Andersen, S. O.: The large contribution of projected HFC emissions to future climate forcing, Proc. Natl. Acad. Sci. USA, 106, 10949–10954, 2009.

ACPD
12, 23829–23911, 2012

Wang, Y. M., Lean, J. L., and Sheeley Jr., N. R.: Modeling the Sun's magnetic field and irradiance since 1713, Astrophys. J., 625, 522–538, doi:10.1086/429689, 2005.
Wielicki B. A., Wong, T., Allen, R. P., Slingo, A., Kiehl, J., Soden, B. J., Gordon, C. T., Miller, A. J., Yang, S.-K., Randall, D. A., Robertson, F., Susskind, J., and Jacobowitz, H.: Evidence for large decadal variability in the tropical mean radiative energy budget, Science, 295, 841–844, doi:10.1126/science.1065837, 2002.
Wigley, T. M. L., Ammann, C. M., Santer, B. D., and Raper, S. C. D.: Effect of climate sensitivity on the response to volcanic forcing, J. Geophys. Res., 110, D09107, doi:10.1029/2004JD005557, 2005a.
Wigley, T. M. L., Ammann, C. M., Santer, B. D., and Taylor, K. E.: Comment on "Climate forcing by the volcanic eruption of Mount Pinatubo" by David H. Douglass and Robert S. Knox, Geophys. Res. Lett., 32, L20709, doi:10.1029/2005GL023312, 2005b.
Willis, D. K.: Can in situ floats and satellite altimeters detect long-term changes in Atlantic Ocean overturning?, Geophys. Res. Lett., 37, L06602, doi:10.1029/2010GL042372, 2010.
WMO (World Meteorological Organization): Scientific Assessment of Ozone Depletion: 2010, Global Ozone Research and Monitoring Project – Report # 52, Geneva, 2011.
Wolter, K. and Timlin, M. S.: El Niño/Southern Oscillation behaviour since 1871 as diagnosed in an extended multivariate ENSO index (ME I.ext), Int. J. Climatol., 31, 1074–1087, doi:10.1002/joc.2336, 2011.
Wu, L. and Liu Z.: Decadal variability in the North Pacific: the Eastern North Pacific mode, J. Clim., 16, 3111–3131, 2003.
Zanchettin, D., Timmreck, C., Graf, H.-F., Rubino, A., Lorenz, S., Lohmann, K., Kruger, L., and Jungclaus, J. H.: Bi-decadal variability excited in the coupled ocean-atmosphere system by strong tropical volcanic eruptions, Clim. Dyn., 39, 419–444, doi:10.1007/s00382-011-1167-1, 2012.
Zhang, R., Delworth, T. L., and Held, I. M.: Can the Atlantic Ocean drive the observed multidecadal variability in Northern Hemisphere mean temperature?, Geophys. Res. Lett., 34, L02709, doi:10.1029/2006GL028683, 2007.
Zhang, Y. and Delworth, T. L.: Impact of the Atlantic Multidecadal Oscillation on North Pacific climate variability, Geophys. Res. Lett., 34, L23708, doi:10.1029/2007GL031601, 2007.
Zhang, Y., Wallace, J. M., and Battisti, D. S.: ENSO-like interdecadal variability: 1900–93, J. Clim., 10, 1004–1020, 1997.

ACPD
12, 23829–23911, 2012

Table 1. Maximum cooling due to Mt. Pinatubo for all model simulations.

SOD GISS	$\Delta T_{\text{PINATUBO}}$			
Surface Temperature Record	NO AMO	Had3 SST	Had3 LIN	Had3 AF
CRU4, global	−0.33	−0.27	−0.15	−0.15
GISS, global	−0.37	−0.32	−0.22	−0.22
NCDC, global	−0.27	−0.23	−0.15	−0.15
CRU4, land	−0.55	−0.44	−0.29	−0.35
GISS, land	−0.40	−0.38	−0.30	−0.32
NCDC, land	−0.50	−0.40	−0.25	−0.28
BEG, land	−0.56	−0.41	−0.25	−0.30
Lower Atmos. Temperature Record				
MSU, global	−0.41	−0.39	−0.33	−0.31
MSU, land	−0.50	−0.46	−0.37	−0.36

ACPD
12, 23829–23911, 2012

Table 2. Values of reduced chi-squared (Eq. 7) calculated for all model simulations.

SOD GISS	χ^2			
Temperature Record	NO AMO	Had3 SST	Had3 LIN	Had3 AF
CRU4, global	1.64	1.34	0.89	0.66
GISS, global	7.03	6.07	4.48	3.71
NCDC, global	6.52	5.65	4.28	3.42
CRU4, land	3.36	2.32	1.62	1.69
GISS, land	14.5	12.1	9.34	8.99
NCDC, land	2.51	1.81	1.39	1.41
BEG, land	45.3	29.9	26.0	26.1
Lower Atmos. Temperature Record				
MSU, global	10.5	7.54	6.19	6.08
MSU, land	18.6	12.8	9.73	9.80

ACPD
12, 23829–23911, 2012

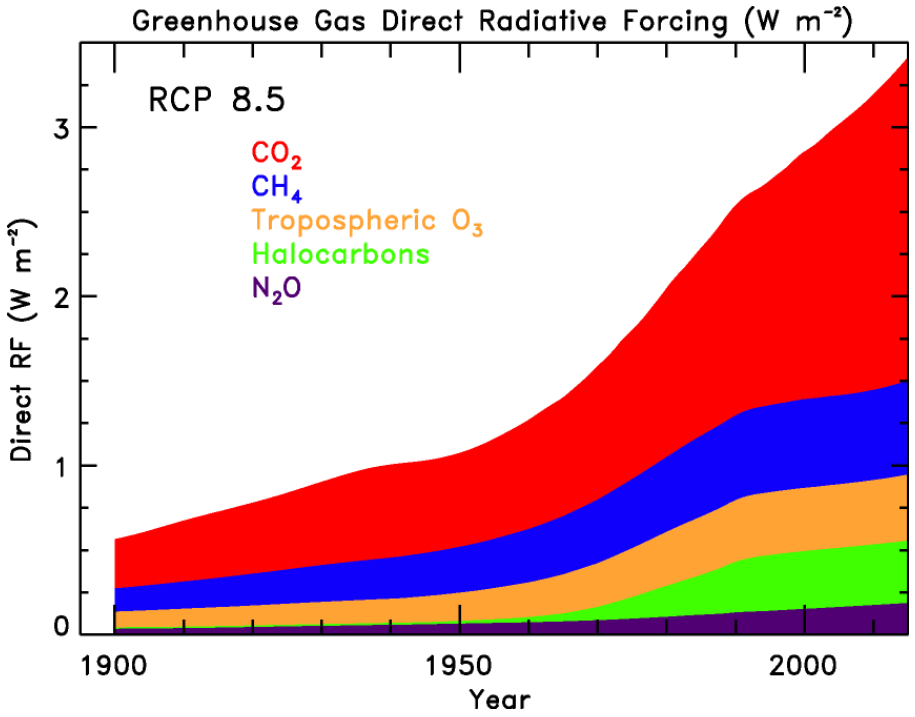

Fig. 1. Direct RF due to greenhouse gases (GHG RF) used as input for all model calculations. The colored regions show individual contributions from CO_2 (red), CH_4 (blue), tropospheric O_3 (orange), halocarbons (green), and N_2O (purple), all based on global, monthly mean mixing ratios from the RCP 8.5 scenario.

ACPD
12, 23829–23911, 2012

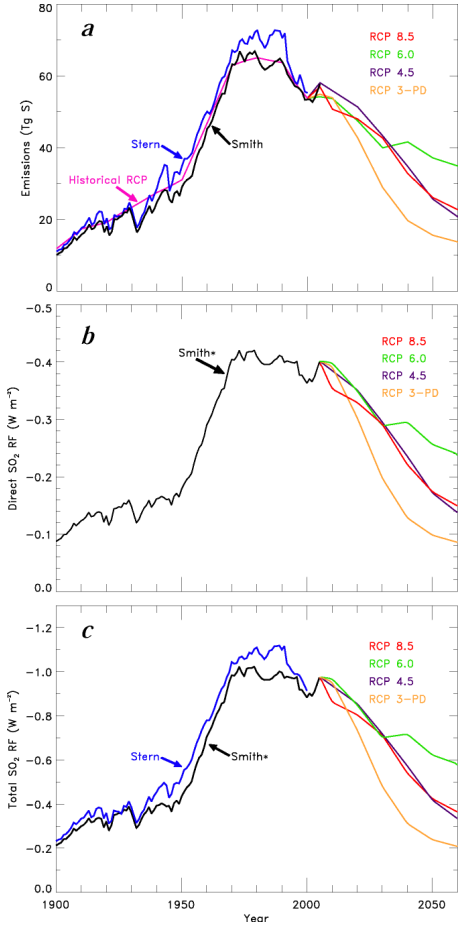

Fig. 2. See caption on next page.

ACPD
12, 23829–23911, 2012

Fig. 2. (a) Global, annual anthropogenic emission of sulfur (S_{EMISS}) from RCP Potsdam compared to values published by Stern (2006b) and Smith et al. (2011). **(b)** Direct RF due to sulfate aerosols ($RF_{SULATE-DIR}$) from RCP Potsdam (post 2005) and the estimate of $RF_{SULATE-DIR}$ (1900 to 2005) used in our model, labeled Smith*, which is tied to S_{EMISS} from Smith et al. (2011) and the IPCC (2007) estimate of $-0.4\,W\,m^{-2}$ for year 2005. **(c)** Total RF due to sulfate aerosols ($RF_{SULATE-TOT}$) from David Stern, Australian National University, provided at the URL given in Appendix B, compared to the value of $RF_{SULATE-TOT}$ used in our model, labeled Smith*, found by multiplying Smith* $RF_{SULATE-DIR}$ by α_{COOL}, for a value of $\alpha_{COOL} = 2.4$, chosen to yield match our estimate of $RF_{SULATE-TOT}$ of $-0.96\,W\,m^{-2}$ for year 2005. Panels are all extended to 2060 for illustrative purposes, to support the statement in the paper that tropospheric aerosol forcing of climate will be diminishing over time.

ACPD
12, 23829–23911, 2012

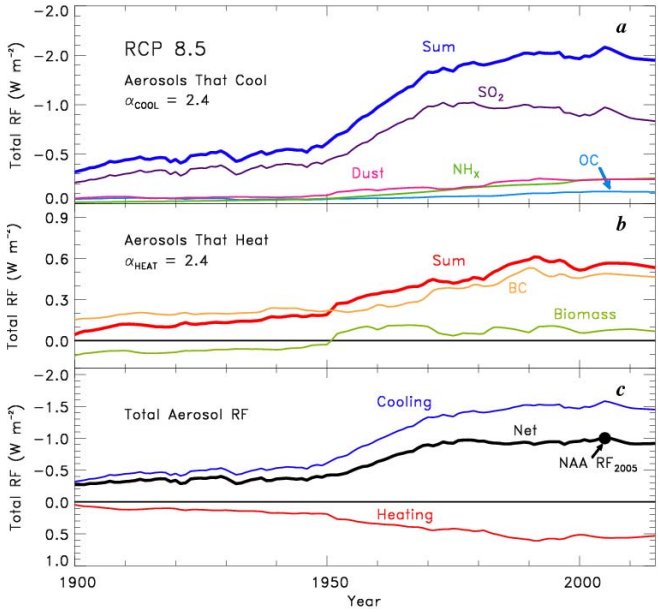

Fig. 3. (a) Total RF of tropospheric aerosols that cool, as labeled, based on our Smith* estimate of $RF_{SULATE-DIR}$ and RCP 8.5 estimates of direct RF for other components, all multiplied by $\alpha_{COOL} = 2.4$. The curve labeled Sum denotes total RF due to aerosols that cool. **(b)** Same as **(a)**, except for aerosols that heat. Direct RF components, from RCP 8.5, have been multiplied by $\alpha_{HEAT} = 2.4$, chosen so that net anthropogenic aerosol RF (NAA RF) in year 2005 equals $-1.0\,W\,m^{-2}$ (IPCC, 2007). The curve labeled Biomass refers to emissions of OC and BC due to biomass burning, and the curves labeled OC and BC refer to fossil fuel burning emissions of these components. **(c)** total RF of aerosols that cool (blue, found for $\alpha_{COOL} = 2.4$), of aerosol that heat (red, found for $\alpha_{HEAT} = 2.4$), and their difference that defines NAA RF (black curve). The value of NAA RF in year 2005 is marked. It is coincidence that the two scaling parameters both require a value of 2.4 to match IPCC (2007) estimates of $RF_{SULATE-DIR}$ and NAA RF in year 2005. Model results are shown for a variety of values of α_{COOL} and α_{HEAT}.

ACPD
12, 23829–23911, 2012

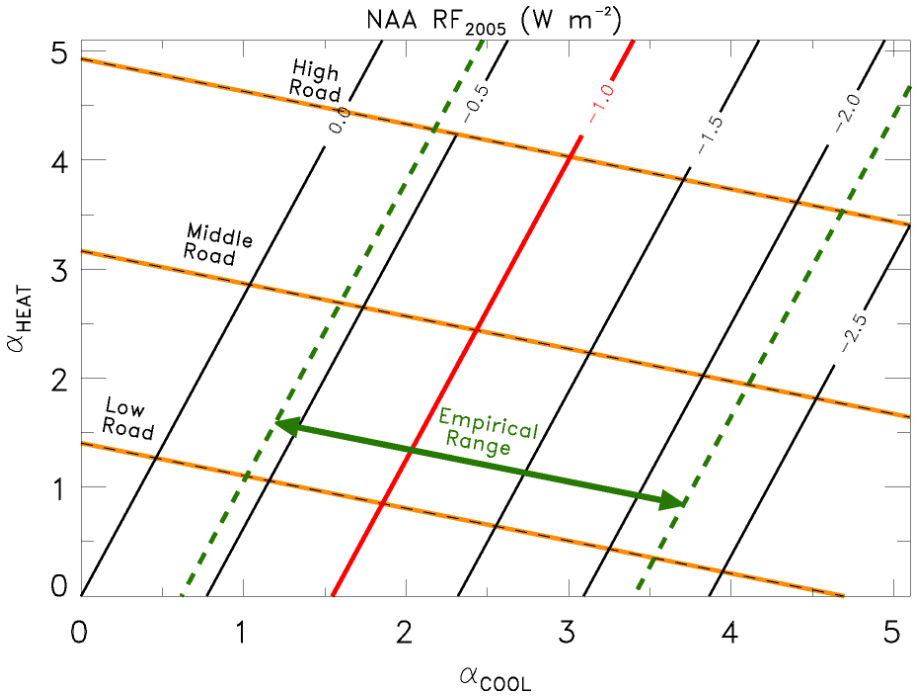

Fig. 4. Contours of net anthropogenic aerosol RF in year 2005 (NAA RF_{2005}) (black solid lines) as a function of α_{COOL} and α_{HEAT}, scaling parameters used to relate direct RF of aerosols to total RF. The contour for NAA $RF_{2005} = -1.0\,W\,m^{-2}$, the best estimate from IPCC (2007), is shown in red. The dashed green lines denote the range of NAA RF_{2005} inferred from data analyses given in Table 2.12 of IPCC (2007) (Appendix D). The black dashed/yellow highlight lines denote various manners upon which values of NAA RF_{2005}, ranging from the lower limit of $-2.2\,W\,m^{-2}$ to the upper limit of $-0.4\,W\,m^{-2}$, can be sampled.

ACPD
12, 23829–23911, 2012

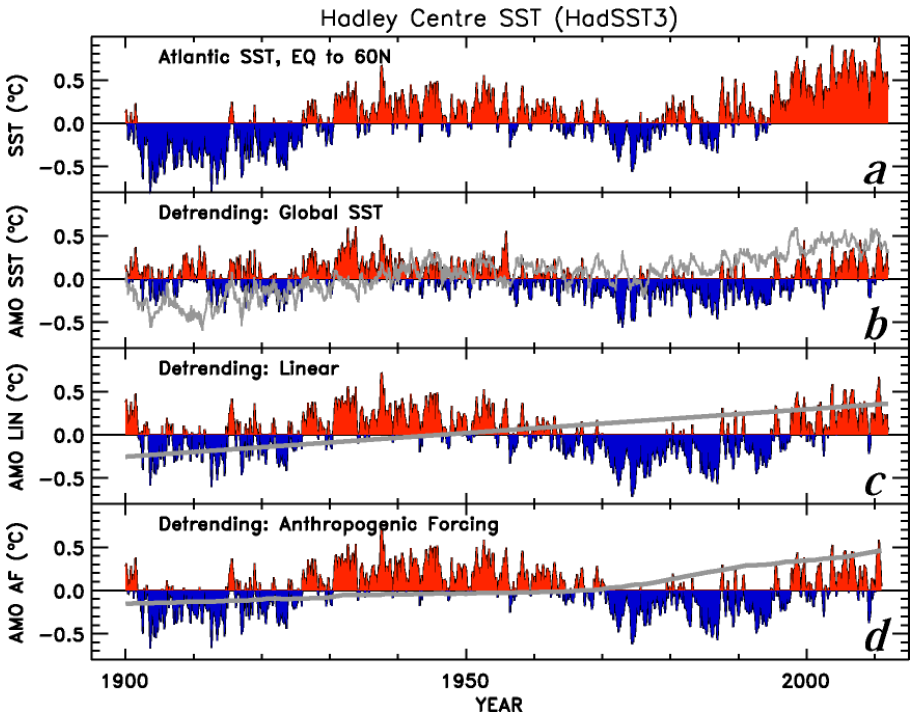

Fig. 5. (a) Area weighted, monthly mean SST in the North Atlantic (equator to 60° N) based on HadSST3 data. **(b)** AMO index (blue and red) found by detrending North Atlantic SST using area weighted SST between 60° S and 60° N (gray curve). **(c)** AMO index (blue and red) found by calculated by detrending North Atlantic SST using a linear regression (gray line). **(d)** AMO index (blue and red) found by detrending North Atlantic SST using anthropogenic RF of climate (gray line). The particular anthropogenic RF curve is an MLR simulation constrained to match the CRU4 global temperature record, NAA $RF_{2005} = -1.0\,W\,m^{-2}$ along the Middle Road, and OHC from Church et al. (2011).

ACPD
12, 23829–23911, 2012

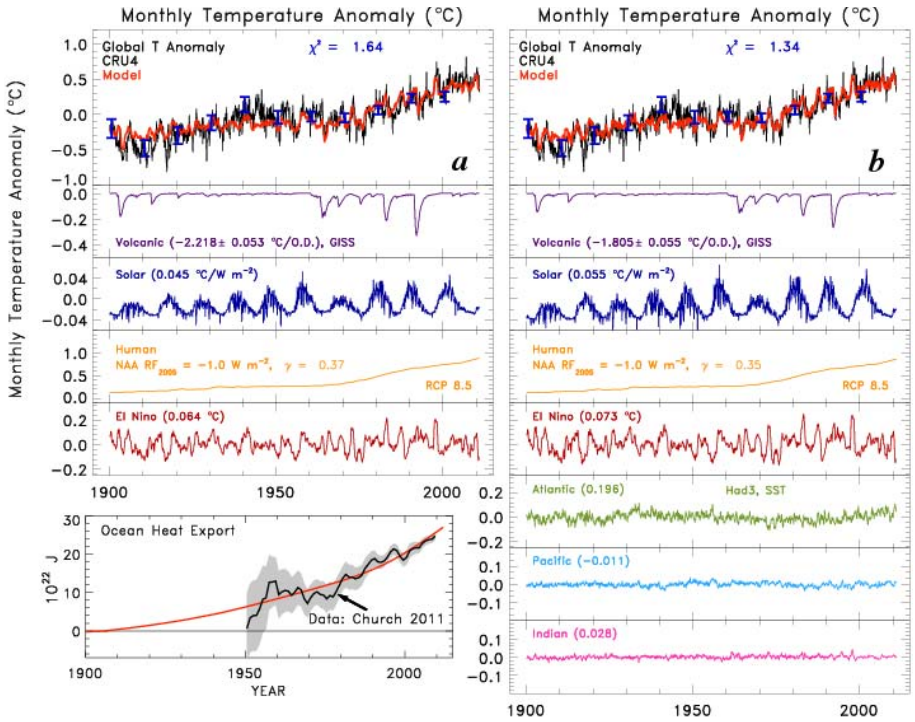

Fig. 6. Ladder plots showing the MLR simulation of the global temperature anomaly from CRU4. The top rung of each of the four ladder plots compares measured (black) and modeled (red) ΔT, from the start of 1900 to the end of 2010. Values of χ^2 are given and 1-sigma uncertainty of ΔT, available for every month, is shown periodically (blue error bars). The other rungs show contributions to ΔT from volcanoes (based on SOD), solar (based on TSI), humans (sum of GHG RF and NAA RF terms in Eq. (2)), and the various ocean terms (see text). Values of the regression coefficients are given; for the volcanic coefficient, the statistical uncertainty from the regression is also presented. Specified values of NAA RF_{2005} and output values of the sensitivity parameter are given in the rung labeled Human. **(a)** (Top) Results of MLR for a simulation where the regression coefficients for AMO, PDO, and IOD have been set to zero. (Bottom) Modeled and measured ocean heat content. Data are from Church et al. (2011). **(b)** Same as top part of **(a)** but also including rungs showing contribution to the regression from variations in SST within the Atlantic (based on $AMO_{Had3\ SST}$), Pacific (PDO), and Indian (IOD) Oceans. **(c)** Same as **(b)** but for $AMO_{Had3\ LIN}$. **(d)** Same as **(b)** but for $AMO_{Had3\ AF}$.

ACPD
12, 23829–23911, 2012

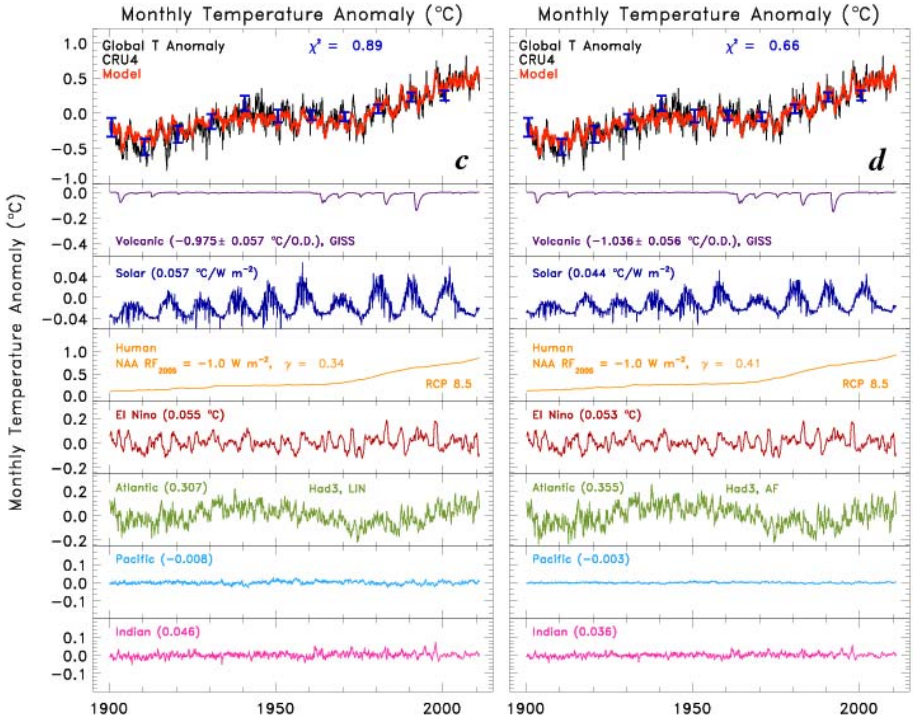

Fig. 6. Continued.

ACPD
12, 23829–23911, 2012

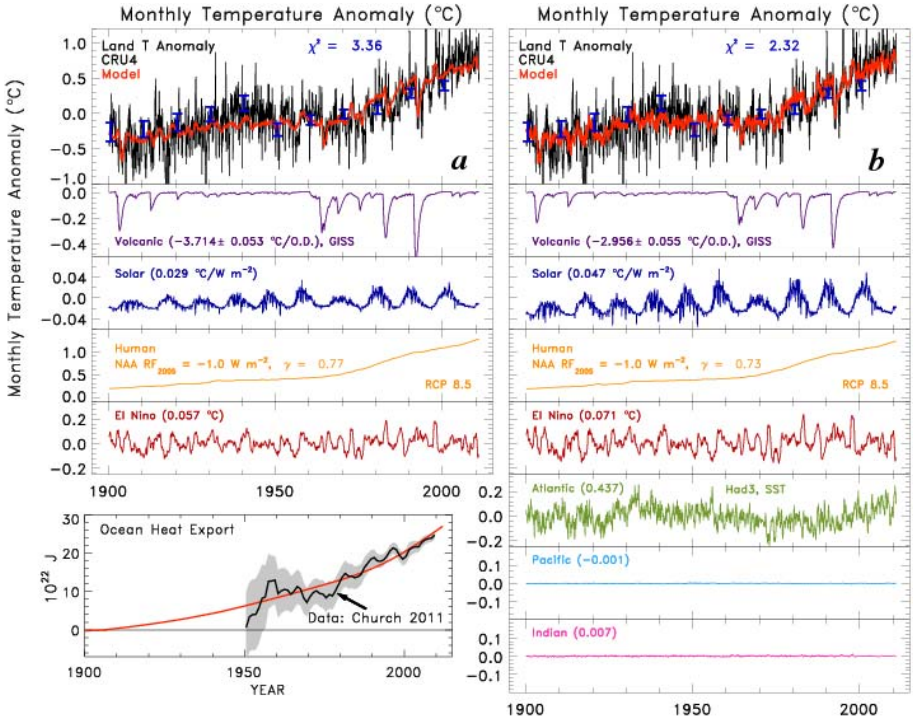

Fig. 7. Same as Fig. 6, but for MLR simulation of the land temperature anomaly from CRU4.

ACPD
12, 23829–23911, 2012

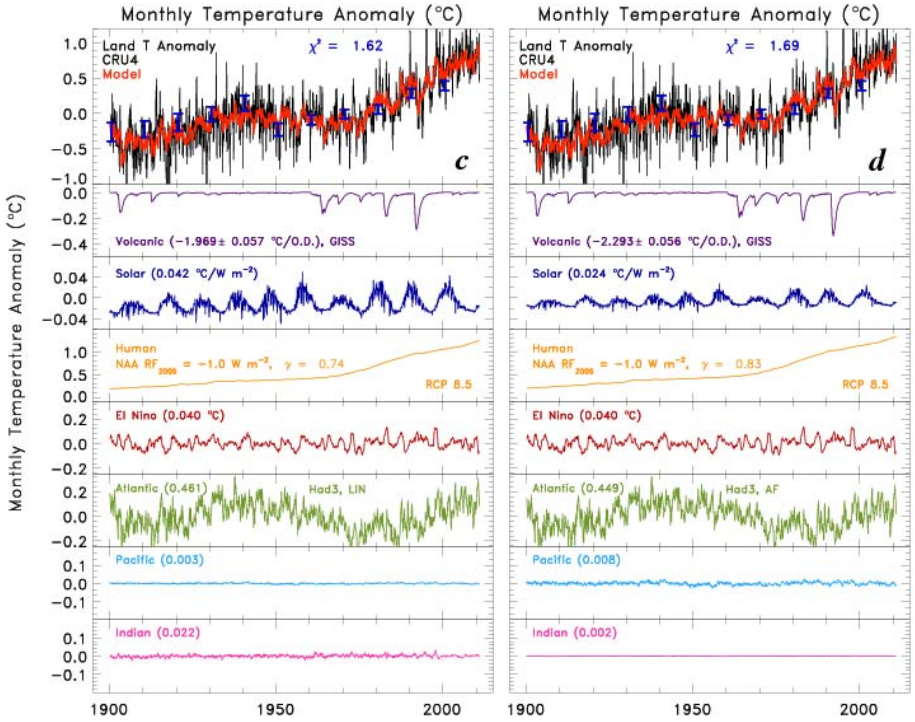

Fig. 7. Continued.

ACPD
12, 23829–23911, 2012

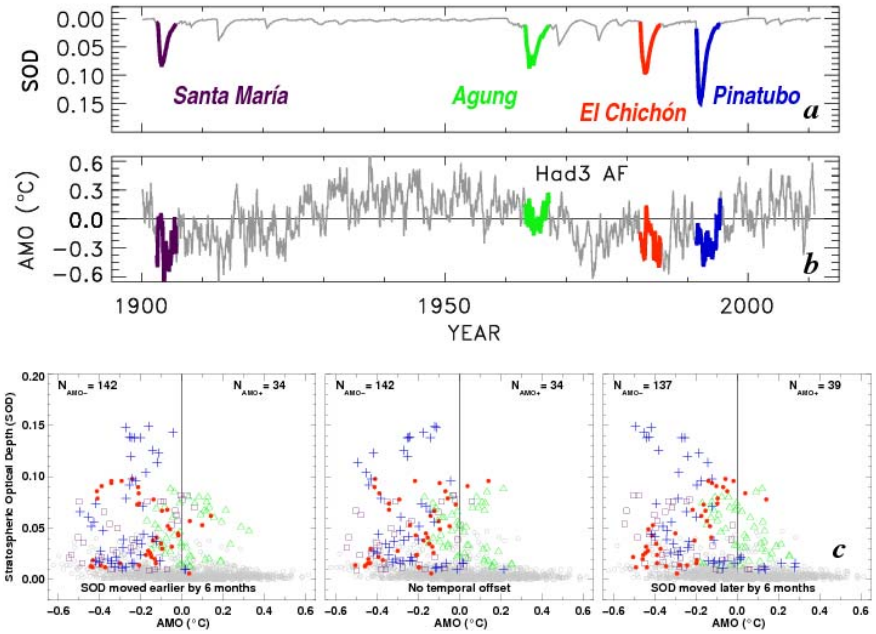

Fig. 8. (a) Monthly mean stratospheric optical depth (SOD) from Sato et al. (1993). The four major volcanoes, Santa Marí a (purple), Mount Agung (green), El Chichón (red), and Mount Pinatubo (blue) are indicated. **(b)** Monthly mean Atlantic Multidecadal Oscillation calculated by detrending HadSST3 using anthropogenic radiative forcing ($AMO_{Had3\ AF}$). Line is same as shown in Fig. 5d except AMO data during the times SOD exceeded 0.01, following the four major volcanic eruptions since 1900, are colored as in **(a)**. **(c)** Scatter plots of SOD versus AMO. In the center, SOD is plotted versus AMO with no time shift. Data collected during the four major volcanic eruptions since 1900 are colored as in **(a)**. The numerical values on the top of the plot tabulate the number of months the AMO index was either positive or negative, when SOD exceeded 0.01 after these four major eruptions. The left hand panel shows a scatter plot for a shift of SOD six months earlier in time and the right hand panel shows a scatter plot for a shift of SOD six months later in time.

ACPD
12, 23829–23911, 2012

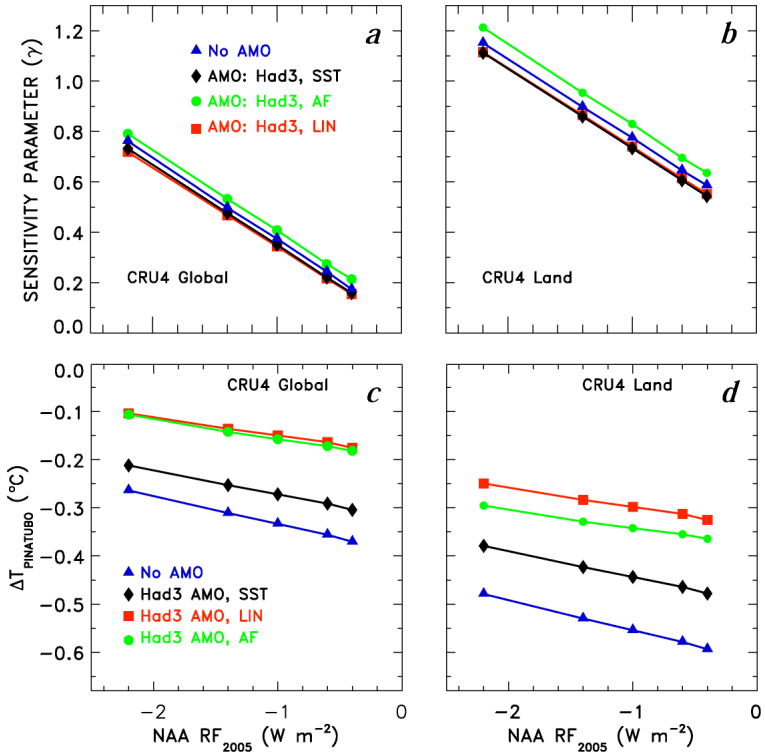

Fig. 9. (a) Sensitivity parameter (γ in Eq. (2)) found for a regression of monthly mean global surface temperature anomaly from CRU4, as a function of NAA RF_{2005} (using values of α_{COOL} and α_{HEAT} along the "Middle Road" of Fig. 4), for different treatments of the AMO: none, $AMO_{Had3\ SST}$, $AMO_{Had3\ LIN}$, and $AMO_{Had3\ AF}$. **(b)** Same as **(a)** except for a regression of the CRU4 monthly mean land surface temperature anomaly. **(c)** Maximum cooling due to the eruption of Mount Pinatubo found by the regression of monthly mean global surface temperature anomaly from CRU4 as a function of NAA RF_{2005} for different treatments of the AMO. **(d)** Same as **(c)** except for a regression of CRU4 monthly mean land surface temperature anomaly.

ACPD
12, 23829–23911, 2012

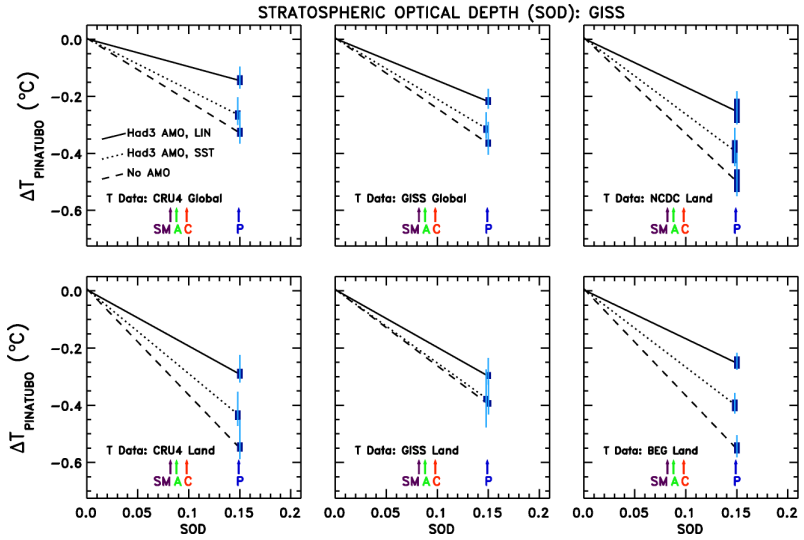

Fig. 10. Cooling attributed to volcanoes ($\Delta T_{\mathrm{VOLCANO}}$) as a function of stratospheric optical depth (SOD), for regression of monthly mean global temperature anomalies (ΔT) from various data centers, as indicated (after "T Data:"). The black lines each represent $C_1 \times$ SOD versus SOD, where C_1 is the volcanic regression coefficient. Results for no AMO (solid lines), $\mathrm{AMO}_{\mathrm{Had3\ LIN}}$ (dotted), and $\mathrm{AMO}_{\mathrm{Had3\ SST}}$ (dashed), assuming NAA $\mathrm{RF}_{2005} = -1.0\,\mathrm{W\,m^{-2}}$ along the "Middle Road" of Fig. 4, are shown for each panel. Maximum SOD associated with the eruptions of Santa María, Mount Agung, El Chichón, and Mount Pinatubo from Sato et al. (1993) are denoted on each panel by the colored arrows marked SM, A, C, and P. The thick dark blue vertical error bars denote the statistical uncertainty in C_1, found by accounting for uncertainties ΔT (Appendix C). The thin blue lines are a root sum of squares combination of the statistical uncertainty and the variation in C_1 due to uncertainty in NAA RF_{2005} (see text). All regressions begin at January 1900. The end date is driven by availability of data. Regressions using data from GISS and NCDC extend to December 2011, regressions using data from CRU4 extend to December 2010, and the regression using data from BEG runs to May 2010.

ACPD
12, 23829–23911, 2012

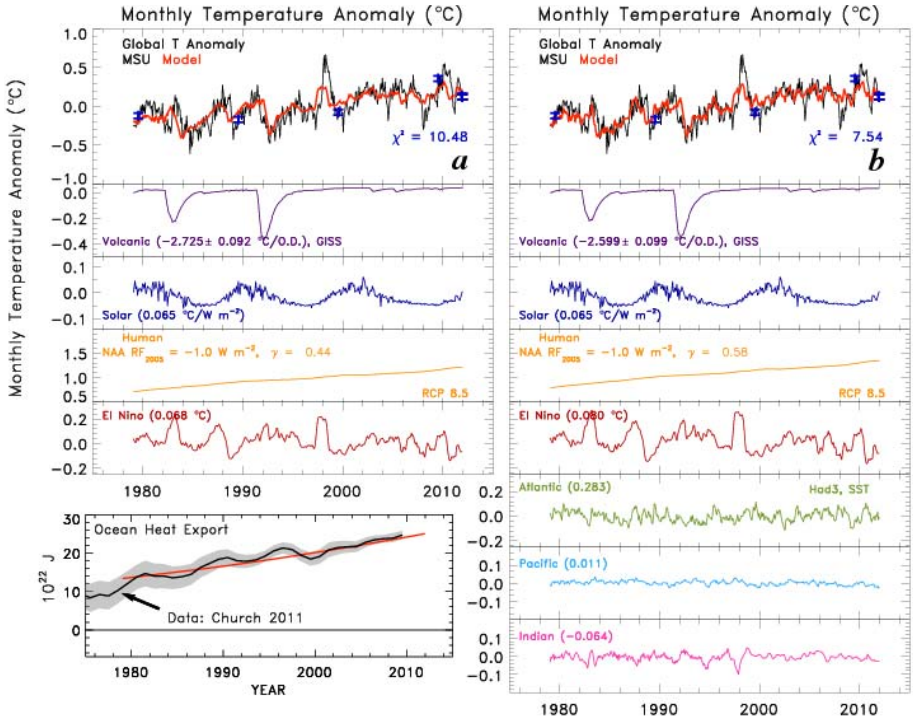

Fig. 11. Same as Fig. 6, but for analysis of the global, monthly mean LT5.4 (lower troposphere) temperature anomaly measured by Microwave Sounding Unit (MSU) instruments. The analysis is from December 1978 to December 2011.

ACPD
12, 23829–23911, 2012

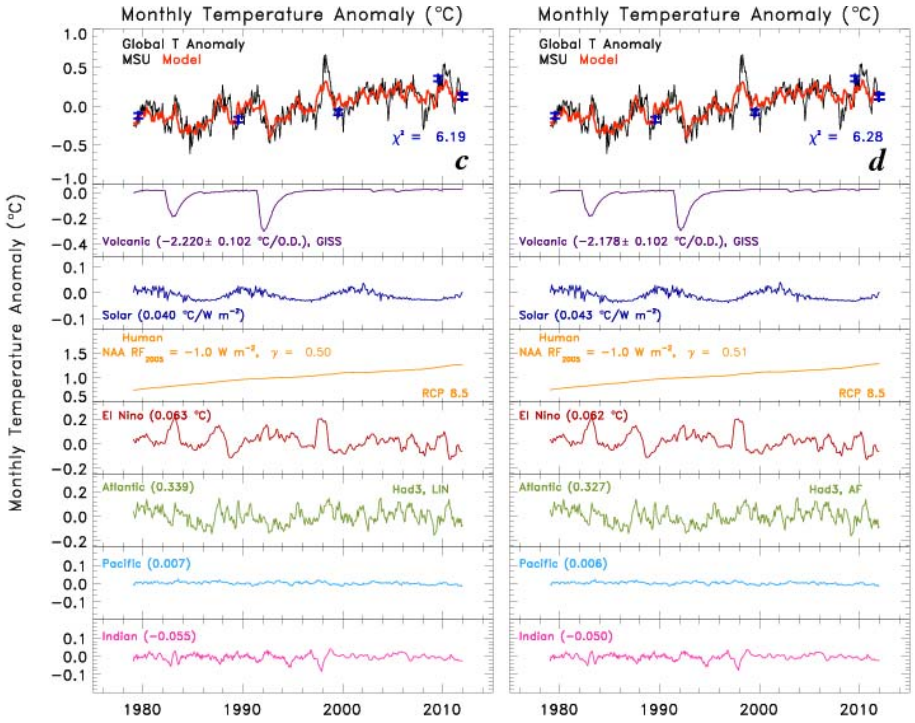

Fig. 11. Continued.

ACPD
12, 23829–23911, 2012

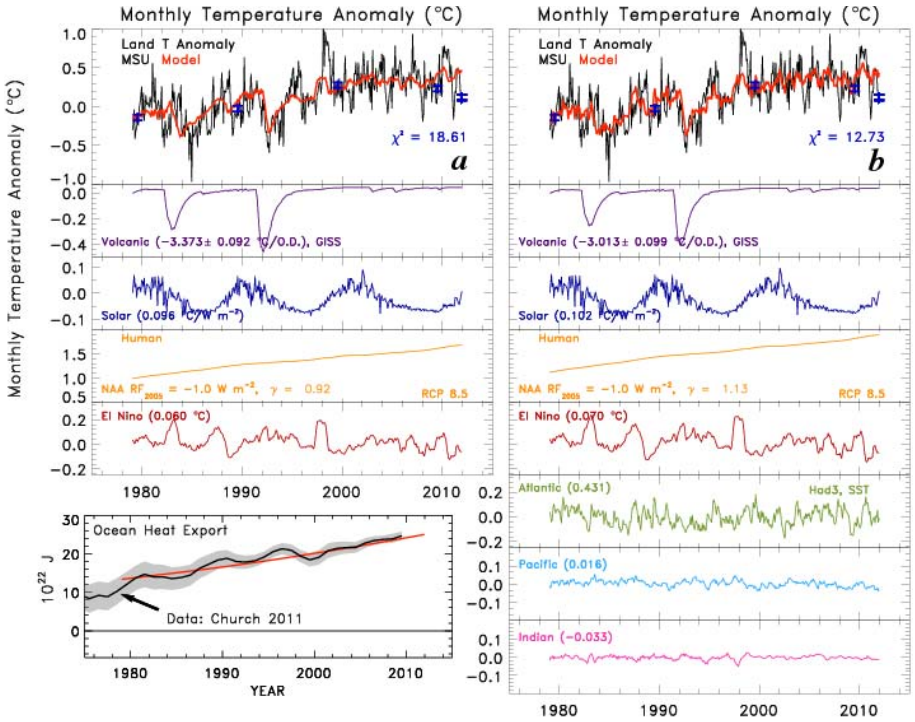

Fig. 12. Same as Fig. 11, but for the MSU land, monthly mean lower troposphere temperature anomaly.

ACPD
12, 23829–23911, 2012

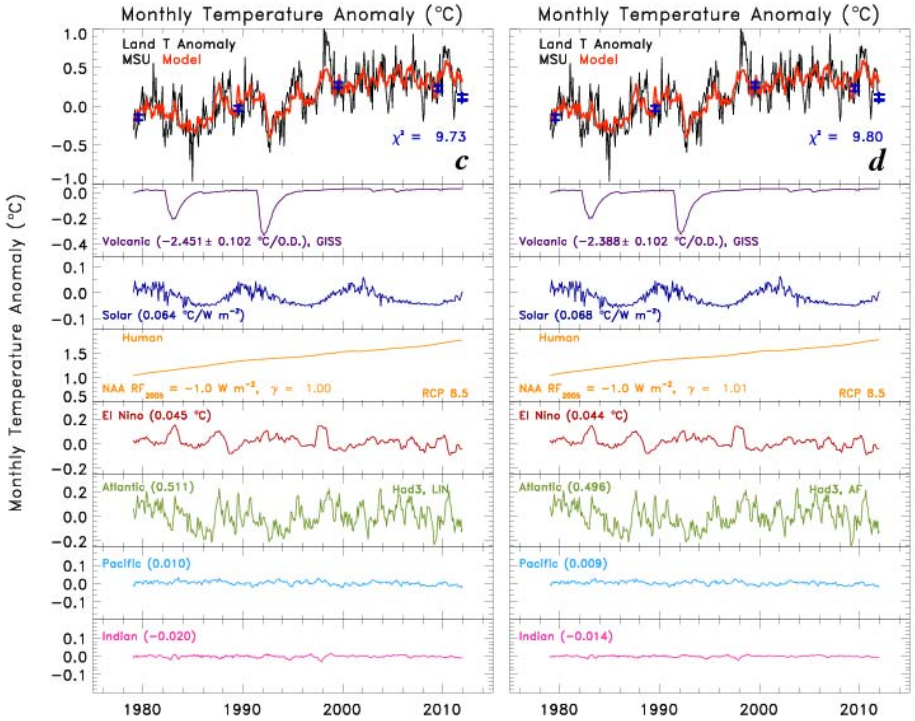

Fig. 12. Continued.

ACPD
12, 23829–23911, 2012

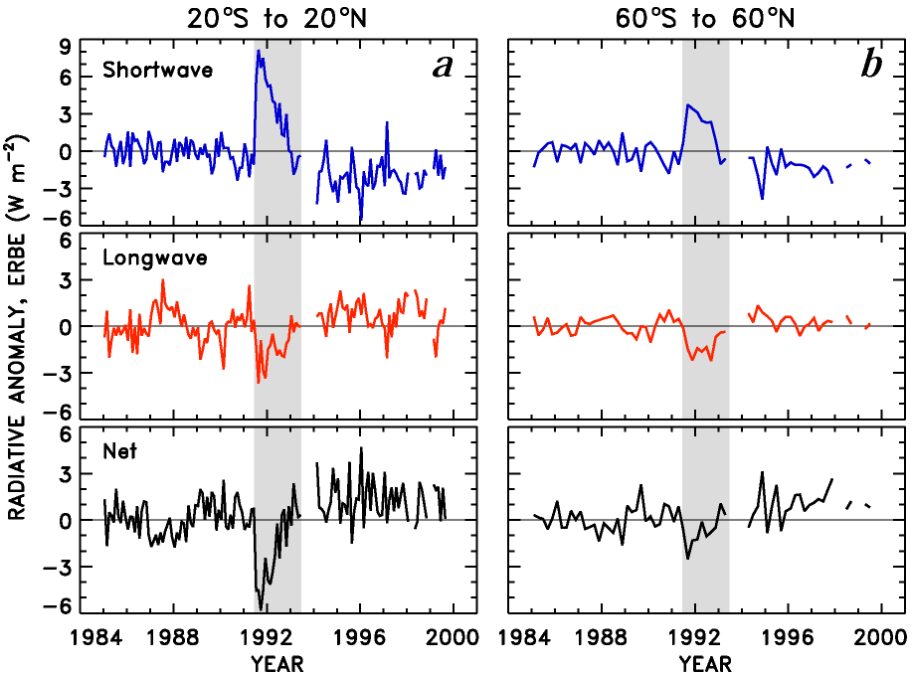

Fig. 13. (a) Deseasonalized times series of shortwave, longwave, and net radiation anomalies for 20° N to 20° S, from the start of 1985 to end of 1999, with respect to a 1985 to 1989 (pre-Pinatubo) baseline. Data are from ERBE Edition 3 Revision 1, non-scanner, wide-field-of-view observations (Wielicki et al., 2002). The gray shaded region denotes the period of time from the eruption of Pinatubo (15 June 1991) until the end of 1992. For this latitude region, raw data are provided as 36-day means**. (b)** Same as **(a)** but for 60° N to 60° S. For this latitude region, raw data from the tropics (36-day means) have been combined with raw data from the extra-tropics (72-day means; extra-tropics refer to 20° to 60° in both hemisphere) to produce a 72-day mean, near global average (using latitudinal weighting).

ACPD
12, 23829–23911, 2012